5-2015

Geochemical Characterization of the Mountain Home Geothermal System

Trevor Alex Atkinson
Utah State University

GEOCHEMICAL CHARACTERIZATION OF THE MOUNTAIN HOME GEOTHERMAL SYSTEM

By

Trevor Alex Atkinson

A thesis submitted in partial fulfillment
of the requirements for the degree

of

MASTER OF SCIENCE

in

Geology

Approved:

Dennis L. Newell Major Professor	James P. Evans Committee Member
John W. Shervais Committee Member	Mark R. McLellan Vice President for Research and Dean of the School of Graduate Studies

UTAH STATE UNIVERSITY
Logan, Utah

2015

ABSTRACT

Geochemical Characterization of the Mountain Home Geothermal System

by

Trevor Atkinson, Master of Science

Utah State University, 2015

Major Professor: Dr. Dennis L. Newell
Department: Geology

The Mountain Home (MH) geothermal system of the western Snake River Plain (SRP) magmatic province was discovered in 2012 by the Snake River Geothermal Drilling Project. Artesian flowing water with a temperature of 150°C was encountered at a depth of 1745 m below ground surface (mbgs) and extensive mineralized fracture networks of pectolite-prehnite, calcite, and laumontite were discovered in the recovered core. The objectives of this study are to: 1) describe the thermal and compositional history of past geothermal fluids, and 2) compare these fluids to modern fluids in order to characterize the evolution of the MH geothermal system and the geothermal potential of the western SRP. Core observations, thin section petrography, X-ray diffraction, and Electron Microprobe analyses were performed in order to describe mineral parageneses of various alteration zones. Carbon and oxygen stable isotope ratios along with temperatures of homogenization from fluid inclusions in hydrothermally precipitated calcite were measured along ~100 m of basalt core from 1709-1809 mbgs. The $\delta^{13}C_{PDB}$ values in calcite range from -7.2 to -0.43 ‰ and $\delta^{18}O_{PDB}$ values range between -20.5 and -15.9 ‰. An anomalous zone from 1722-1725 m depth displays a range in $\delta^{13}C_{PDB}$ and

$\delta^{18}O_{PDB}$ of -1.9 to +0.88 ‰ and -17.1 to -8.1 ‰, respectively, suggesting non-equilibrium fractionation due to boiling. Carbon isotopic ratios suggest a mixture of deep-seated mantle derived and meteoric fluids. Fluid inclusion microthermometry has identified primary inclusions with trapping temperatures ranging from 168-368°C. A calcite-water geothermometer used to calculate paleo-fluid oxygen isotopic composition (-0.43 to +7.2 ‰ SMOW) and a comparison with present-day fluid oxygen isotopic composition (-3.2 ‰ SMOW) reveals a cooling trend with potential mixing of meteoric waters and deeply derived fluid. The MH geothermal system has cooled over time and reflects potentially less, if any magmatic fluid input presently into the system as there was in the past.

(104 pages)

PUBLIC ABSTRACT

Geochemical Characterization of the Mountain Home Geothermal System

by

Trevor Atkinson, Master of Science

Utah State University, 2015

Major Professor: Dr. Dennis L. Newell
Department: Geology

The Mountain Home (MH) geothermal system of the western Snake River Plain (SRP) was discovered in 2012 by the Snake River Geothermal Drilling Project. Flowing water with a temperature of 150°C was encountered at a depth of 1745 m below ground surface and extensive mineralized veins were discovered in the recovered core. The objectives of this study are to 1) describe the thermal and compositional history of past geothermal fluids and 2) compare them to those of today in order to more fully understand the evolution of the MH geothermal system and the geothermal potential of the western SRP. Approximately 150 meters of basalt care were analyzed in order to describe mineral occurrences in various alteration zones. Stable isotope geochemistry, along with fluid inclusion measurements in hydrothermal calcite, was also measured. Carbon isotopic ratios suggest mixing of mantle-derived and meteoric fluids. Fluid inclusion measurements have identified past temperatures ranging from 168-368°C. Geothermometry reveals a cooling trend with potential mixing of meteoric waters and

magmatic fluids. The MH geothermal system has cooled over time and reflects potentially less magmatic fluid input into the system as there was in the past.

ACKNOWLEDGMENTS

I have many people to thank for their support and encouragement throughout this project. First and foremost, I would like to thank my advisor Dennis Newell. Without his expertise, input, and suggestions, this would have been very difficult. I thank him for his overwhelming generosity and thoughtfulness in helping me become who I am as a scientist and professional. Much appreciation goes out to the Department of Geology at Utah State University for seeing my potential and supporting me through this research. I also acknowledge the Colorado Scientific Society for their funding and support. My committee, comprised of John Shervais, James Evans, and Dennis Newell, was also indispensible for helping guide the direction of this study. The many faculty members at Utah State University deserve my gratitude for always being generous with their time and resources in order to further my research and professional development. Apart from my committee and faculty at USU, I need to thank Mike Dorais from Brigham Young University for his technical expertise and help using the Electron Microprobe. Above all, I would like to thank my wife Alicia and my two children Ryker and Brinly for sticking by me and supporting me throughout my education. Many hours were spent away from home to complete my research and I am very much indebted to my wife for taking care of our children while I was away. It is impossible to thank all the people who have been integral in making me the person, friend, and scientist that I am today but I hope that you know how much you are appreciated. This project has been enlightening and such a privilege of which to have been apart.

Trevor Atkinson

CONTENTS

Page

LIST OF TABLES

LIST OF FIGURES

Figure Page

1. INTRODUCTION

1.1 OVERVIEW

The Snake River Geothermal Drilling Project (SRGDP), also known as "Project Hotspot", drilled and cored three deep geothermal test holes from 2010-2012. These include the Mountain Home, Kimberly, and Kimama holes (Figure 1). The main objective of the SRGDP was to evaluate the geothermal potential of the Snake River Plain (SRP) in three distinct settings: a faulted graben (Mountain Home hole), the margins of the SRP (Kimberly hole) and the axial volcanic zone (Kimama hole). The Mountain Home hole, which is the principal focus of this study, was drilled in 2011-2012 by Drilling Observation and Sampling of Earth's Continental Crust (DOSECC). It is near the northeast margin of the western SRP approximately 65 km southeast of Boise, Idaho on the Mountain Home Air Force Base. The Kimberly hole is located 10 km southeast of Twin Falls and the Kimama hole is located approximately 40 km north of Burley, Idaho (Figure 1).

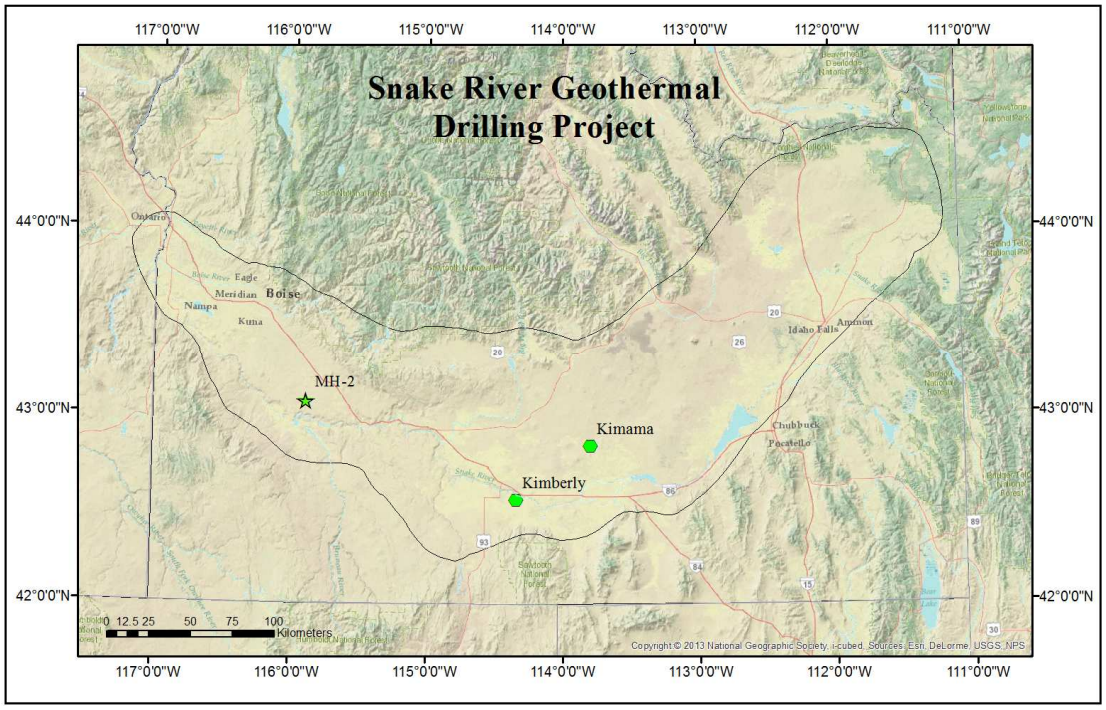

Figure 1: Map of the Snake River Plain (black outline) and the locations of the three holes drilled during the Snake River Geothermal Drilling Project; The Mountain Home (MH-2) hole is the focus of this study. (modified from Nielsen and Shervais, 2014)

1.2 OBJECTIVES

The Mountain Home 2 (MH-2) hole encountered 150°C artesian flowing waters from 1745 mbgs (meters below ground surface) (5276 feet bgs) and core extracted from the hole contains zones of fracture-hosted secondary mineralization in hydrothermally altered basalt. The objective of this study is to understand the thermal and compositional evolution of this unique geothermal system. Important questions that this research will address are: 1) what were the past thermal regimes of the geothermal system and how do they compare to today's hydrothermal temperature? and 2) what was the source and isotopic composition of the paleo-fluids responsible for mineralization? I hypothesize that the secondary mineralization in the core was precipitated during past circulation of

geothermal fluids and that these minerals record past geochemical and thermal conditions of a magmatic-hosted geothermal system. Stable isotope analysis, fluid inclusion microthermometry, and microscopy of the mineralization are synthesized to compile a high-resolution record of past fluid temperatures and chemistry. Understanding thermal and compositional evolution of the geothermal fluids is critical for further geothermal exploration in the Snake River Plain. (Armstrong et al., 2013)

1.3 SIGNIFICANCE

The MH geothermal system lies in the subsurface below the Mountain Home Air Force Base and therefore has the potential to provide needed energy for the base and surrounding areas. Providing an evolutionary history and characterization strategy of the MH geothermal system will help to explain this basalt-hosted geothermal system and provide a wealth of information regarding basalt-hosted geothermal systems that lack usual surface manifestations. The characterization strategy presented here may also provide a framework for investigating and identifying other 'blind' geothermal resources of the western U.S. Such systems are important in recent geothermal research and could hold vast potential for energy production.

2. BACKGROUND

2.1 GEOLOGIC AND HYDROLOGIC SETTING

The SRP volcanic province is in southern Idaho and spans an area of approximately 40,400 km^2 (Lindholm, 1996). Based on volcanic history, stratigraphy, and structural controls, the SRP has been divided into two distinct tectonic terrains: the eastern SRP (ESRP) and the western SRP (WSRP) (Mabey, 1976, 1978, 1982).

2.1.1 Eastern Snake River Plain

The ESRP represents the track of the Yellowstone hot spot from its point of initiation beneath the Owyhee Plateau to its current location in northwest Wyoming (Pierce and Morgan, 1992). From 16 to 2 Mya large caldera-forming eruptions (Figure 2) emplaced much of the silicic material (Heise and Idavada volcanics) that underlies the most recent Quaternary mafic volcanic units.

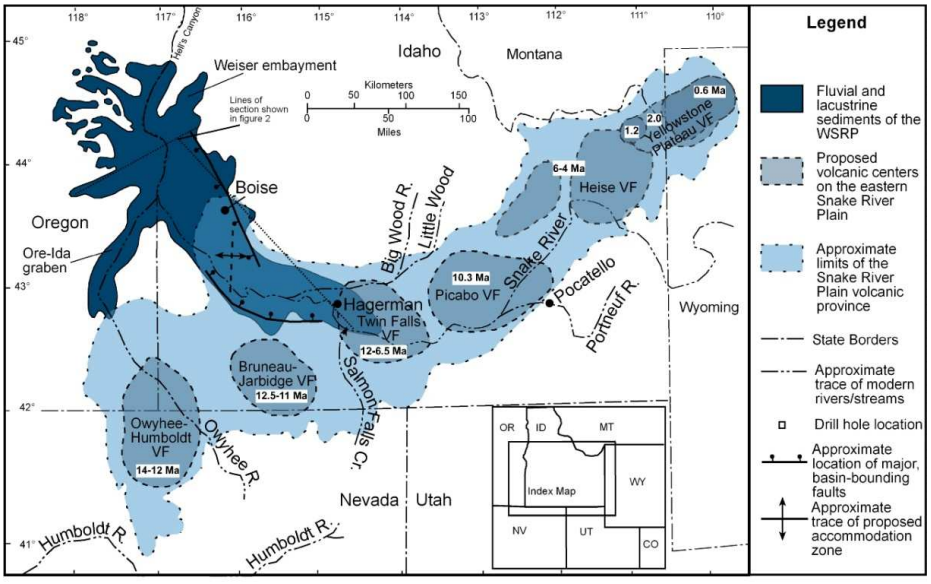

Figure 2: Map of the Snake River Plain volcanic province and major calderas formed from the Yellowstone hot spot migration; The WSRP extends westward from approximately Hagerman to Boise, ID. (modified from Link and Phoenix, 1996)

Geophysical models of the ESRP indicate that this area is a down-warped structural depression with normal-fault control on its margins (Mabey, 1978, Pierce and Morgan, 1992, DeNosaqou et al., 2009). The emplacement of large volumes of melt in mid-crustal regions and near the surface resulted in subsidence and faulting along the margins of the ESRP.

2.1.1.1 Snake River Plain Aquifer

The Snake River Plain Aquifer (SRPA) underlies the ESRP and is one of the most productive aquifers in the United States. It is hosted primarily in Quaternary basalt and ranges between 60-270 m thick. Transmissivity ranges from approximately 930-223,000 m^2/day in the upper 60 m of the aquifer (Lindholm, 1996). Horizontal hydraulic conductivity values vary greatly from less than 20 m/d to 11,000 m/d. Oxygen ($\delta^{18}O$) and hydrogen (δD) isotopic analyses of SRPA ground and surface waters indicate that it is derived primarily from local precipitation (Figure 3, Wood and Low, 1986) plotting along the regional meteoric water line with small variations most likely due to altitude and temperature. The $\delta^{18}O_{SMOW}$ and δD_{SMOW} values range from -19 to -16 ‰ and -125 to -145 ‰, respectively. Recharge of the system typically occurs from the mountains north of the plain and from the Yellowstone plateau to the northeast. Water moves southwestward and is discharged near King Hill and Hagerman, Idaho (Figure 4).

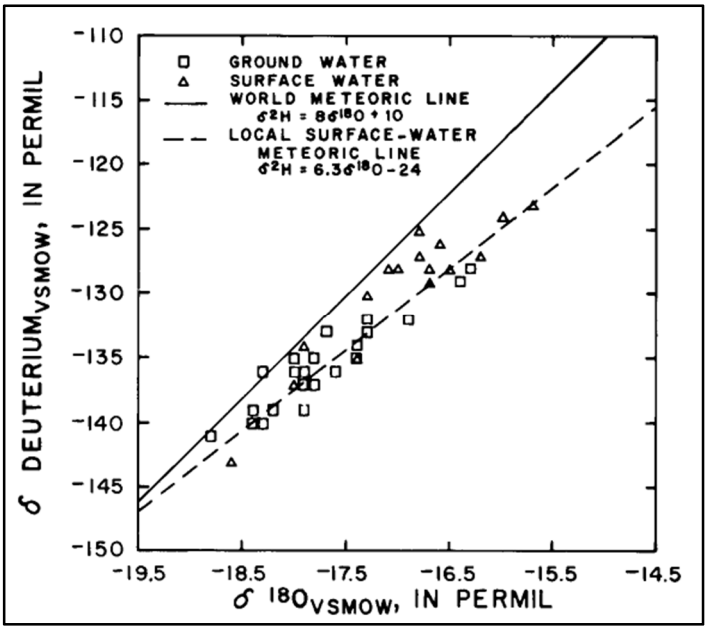

Figure 3: $\delta^{18}O$ and δD of surface and ground waters in the ESRP; (modified from Wood and Low, 1986)

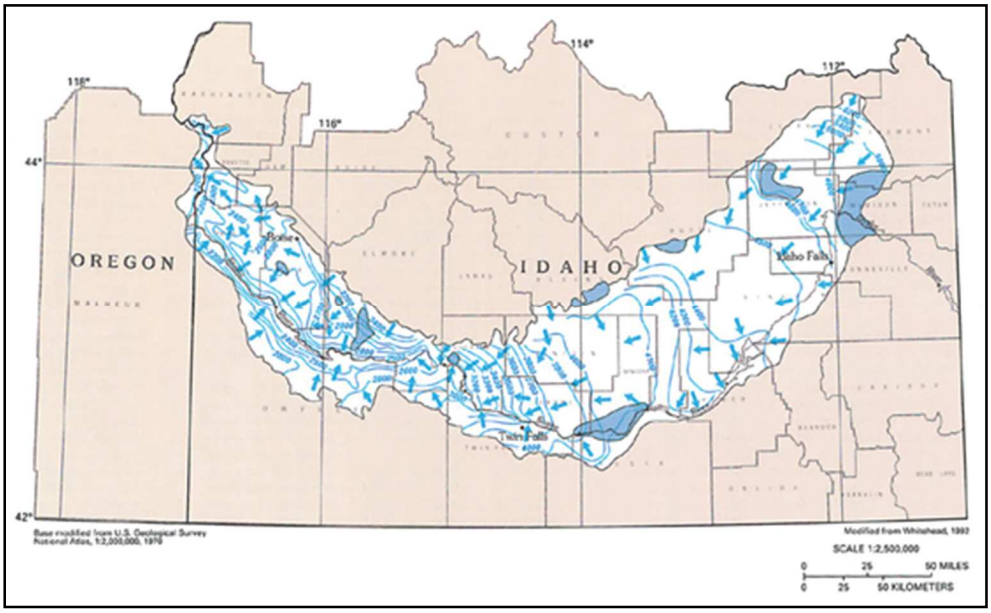

Figure 4: Map of the water table contours and inferred water flow direction throughout the SRPA system; Solid blue areas are perched water aquifers above the SRPA. (modified from Whitehead, 1994)

2.1.2 Western Snake River Plain

The WSRP is a northwest trending graben bounded by en echelon normal faults to the northeast and southwest (Figure 5, Shervais et al., 2002). Volcanic activity in this region began at ~11 Ma with rhyolitic composition eruptions along the flanks of the plain contemporaneous with Basin and Range extension (Ekren, 1982). These serve as the basement rock for subsequent basaltic magmatism that began about 9 Ma and lacustrine sediments (Idaho Group) in the Pliocene-Pleistocene Lake Idaho (Jenks and Bonnichsen, 1989). Basalts younger than 2 Ma exposed as surface flows and shield volcanoes cap the lacustrine sediments (Figure 6, Shervais et al., 2002).

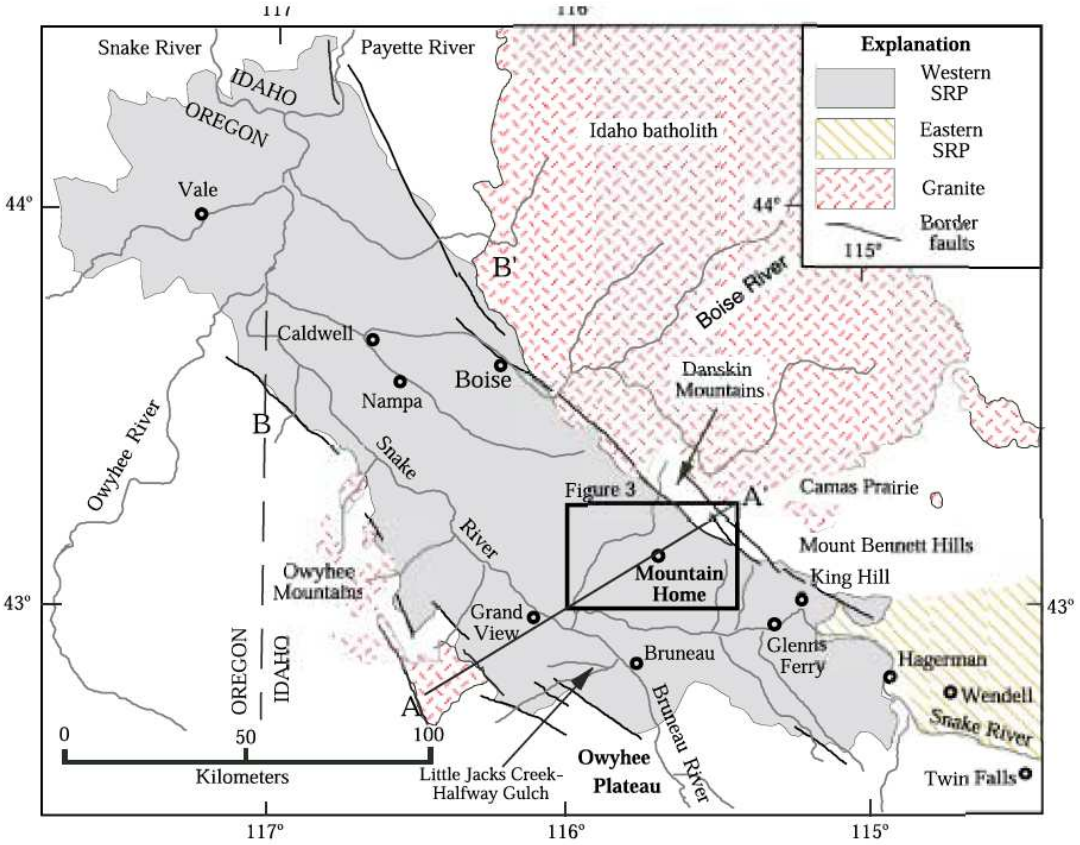

Figure 5: Map of southern Idaho and the western SRP along with adjacent parts of the Idaho batholith; Note the location of Mountain Home (~65 km SE of Boise, 113 km NW of Twin Falls). (modified from Shervais et al., 2002)

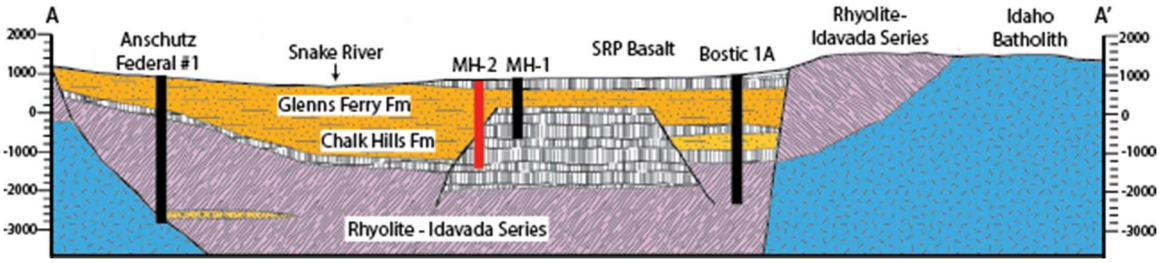

Figure 6: Cross section associated with figure 5 showing the subsurface geology of the WSRP constrained by four deep test holes represented by red (MH-2) and black bars (Bostic 1A, MH-1, and Anschutz Federal #1) (modified from Shervais et al., in press)

2.2 GEOTHERMAL ENERGY

Geothermal energy is derived from natural heat generated within the Earth. This heat originates from two general sources, primordial heat loss from the Earth's core and radioactive decay (Turcotte and Schubert, 2002). It is estimated that the amount of heat produced by the Earth is approximately 47 terawatts (Davies and Davies, 2010). Convection in the mantle and thermal conduction in the crust allow heat to move from interior to the Earth's surface. Once heat is within the crust, it is transferred via multiple mechanisms and usually involves 1) shallow igneous intrusions that provide a long-lived heat source and/or 2) deep seated faults that allow for heated fluids to be transmitted to the upper crust into a geothermal reservoir where it can be extracted (Armstrong et al., 2013).

Geologic factors that must be examined in exploration for an economic geothermal resource include depth, thickness, and extent of the aquifer, rock properties, fluid chemistry, and temperature, porosity and permeability of rock formations (Rummel and Kappelmeyer, 1993). Many of these contribute to the heat flow equation:

$$Q = k\frac{\Delta T}{\Delta x} \qquad (1)$$

where Q is the heat flow through a material (W/m^2), k is the thermal conductivity (W/mK), T is temperature in Kelvin and x is the material thickness. Together, $\Delta T/\Delta x$ is the thermal gradient of a certain region of earth.

Heat flow across the United States varies from 15-150 mW/m^2 (Figure 7) which can be explained in part by relative ages and the variable thickness of Earth's crust (Blackwell et al., 2011). In the eastern U.S., relatively low heat flow values can be attributed to a thicker, older crust of the North American craton and overlying sedimentary units. The western U.S. shows a distinct increase in heat flow within the Basin and Range province where crustal extension has caused extensive faulting and crustal thinning for the last ~17 million years allowing for more facilitated heat flow. The west coast displays some of the lowest values in the country due to subduction of the cold Pacific plate beneath the North American plate. Although the heat flow is low here, due to the partial melting of the overlying crust and emplacement of shallow intrusive rocks, it creates some of the highest quality geothermal resources (e.g. The Geysers and Newberry Caldera). An elevated heat flow trend in east Texas through northern Louisiana and southern Arkansas is attributed to the Ouachita tectonic front which includes many marine shales that have high amounts of radioactive materials which contribute to high heat generation (Negraru et al., 2009). The SRP has an elevated heat flow (80-150 mW/m^2) and is most likely related to a mid-crustal mafic sill complex (Blackwell, 1989) and the thinning of crust due to Basin and Range extension.

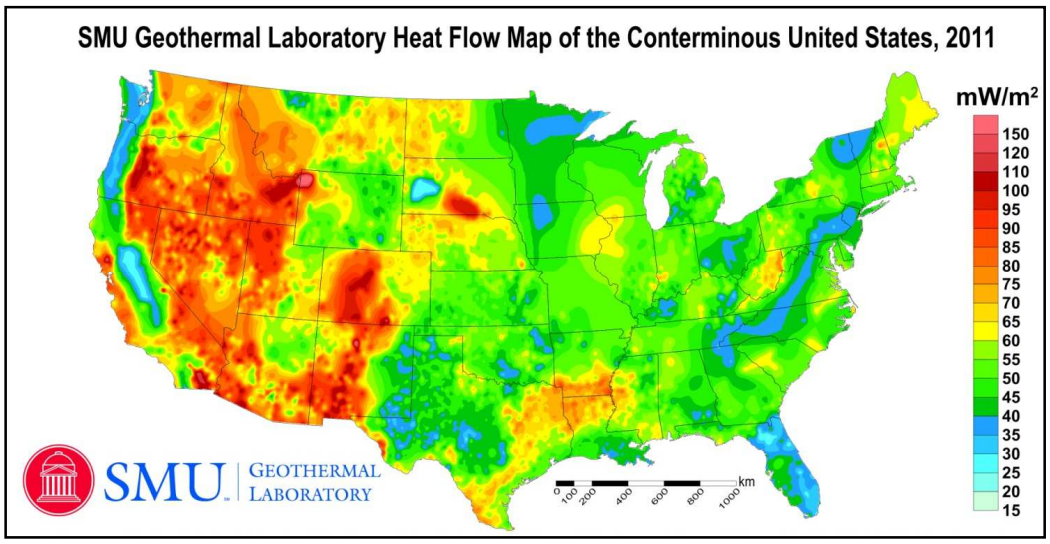

Figure 7: Geothermal heat flow map of the conterminous United States; (Blackwell et al, 2011)

Where high heat flow, and the factors mentioned above are found to be optimal, an exploitable geothermal system may be present. Gupta and Roy (2007), identify five general types of geothermal systems: vapor-dominated, hot water, geo-pressured, hot-dry rock, and magma driven.

Vapor-dominated geothermal systems are often in areas of recent (Miocene-Quaternary) volcanism, attributing shallow, high temperature (500-1000°C) magma intrusions as the heat source. These intrusions heat the surrounding rocks and fluids enough to the boiling point of water and a steam reservoir results (Figure 8). This steam (>150°C) rises to the surface through faults and/or drilled wells and passed through a generator to create electricity at a dry steam power plant (Figure 10). The Geysers in northern California and Larderello, Italy are examples of dry steam geothermal power plants.

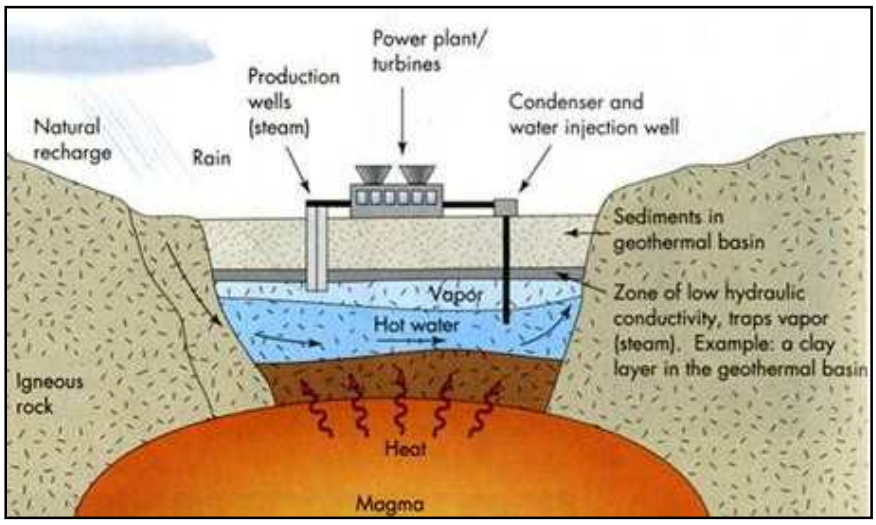

Figure 8: Schematic representation of a vapor-dominated geothermal system; (modified from Keller, 2000).

Water that is heated through conduction from hot rocks and convectively transferred from a deep source to a shallow reservoir characterizes hot water geothermal systems (Figure 9). They differ from vapor-dominated systems in that heated water, not steam, is the pressure controlling fluid (Gupta and Roy, 2007). The reservoir is typically 200°C or more and is present at depths from 1500-3000 m. As the water flows, or is pumped, to the surface, the water flashes to steam due to the rapid pressure decrease and is used to turn generators (Figure 10). Flash steam power plants take advantage of this hot water and are the most common geothermal power plant. An example is in SW Iceland at the Hellisheidi Power Station.

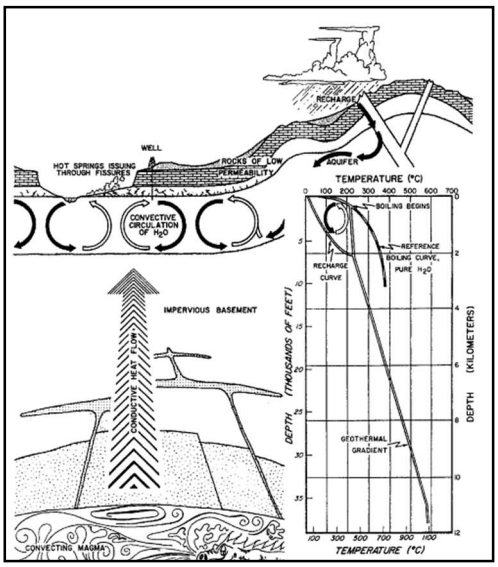

Figure 9: Schematic representation of a hot water geothermal system; Note the absence of steam. (modified from Gupta and Roy, 2007)

At more moderate temperatures (100-180°C), such as the Raft River geothermal system in Idaho, a binary cycle plant is used (Figure 10, Duffield and Sass, 2003). This water is passed through a system in which it flashes a secondary working fluid, typically hydrocarbon based such as butane or pentane, whose boiling point is much lower than that of water. The subsequent vapor produced thereby is used for electricity production. The MH-2 waters flowed at 150°C and would likely be a great candidate for a binary cycle power plant.

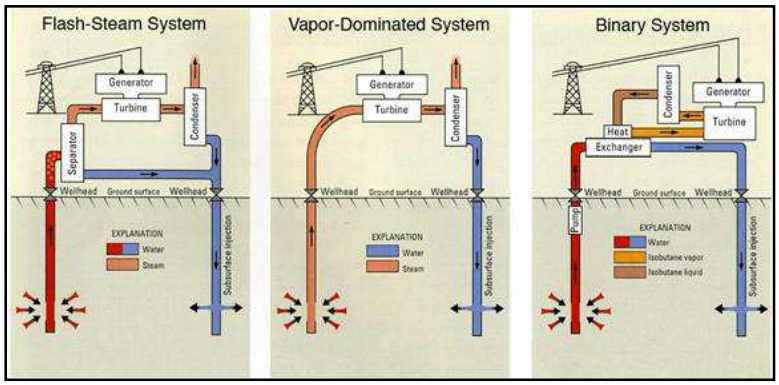

Figure 10: Three diagrams illustrating the different geothermal power plants; (modified from Duffield and Sass, 2003)

Geopressured systems are found in the Gulf of Mexico where hot water is nearly sealed off from exchange with surrounding rocks (Duffield and Sass, 2003). Rapid sediment filling exceeds the fluid expulsion rates and subjects the pore fluids to higher than normal pressures. Normal faulting with high amounts of throw and basin subsidence creates unique juxtapositions of hot and cold rock that also contribute to overpressurized geothermal fluids. These systems typically have temperature ranges from 100-200°C and would likely be candidates for binary geothermal plants.

Hot dry rock systems are within 10 km depth where rocks store heat and do not produce water or steam (Hot Dry Rock Assessment Panel, 1977). The rocks in these systems have low permeabilities, lack appreciable fluid content, and likely exist below all major geothermal systems. Much research has been done at Fenton Hill, near the Valles Caldera near Los Alamos, New Mexico where water was pumped to depth and fractured the rock allowing the heat to exchange with the water and then extracted for exploitation (Duchane and Brown, 2000). Drilling to such depths and pumping large quantities of water was later discouraged based on the cost of drilling and commercial exploitation.

The idea of drilling near a magma body to access high temperatures for high-grade electricity production is not a new one. In 1980, the idea was tested in Hawaii when they drilled into a molten core of a lava lake. Most recently, scientists with the Iceland Deep Drilling Project encountered >900°C magma flowing into a 2.1 km deep well and proved a potential 36 MW of energy from >450°C dry superheated steam (Elders et al., 2014) making this the world's hottest producing geothermal well.

Although, the idea is plausible, the danger and financial implications have made this a less explored type of geothermal system.

2.3 PREVIOUS WORK

2.3.1 Geological Setting and Borehole Lithology

The MH-2 hole was drilled in 2011-2012 on the northwestern corner of the Mountain Home Air Force Base in Elmore County, southwest Idaho approximately 65 km southeast of Boise (lat:43° 4'11.57"N long:115°53'34.61"W, Figure 5). The location of the drill hole was chosen based on multiple observations that suggested good potential for encountering a geothermal resource. This area has an elevated heat flow of approximately 80 mW/m^2 (Blackwell et al., 2011). The Bostic 1A wildcat oil well, ~20 km SE of MH, had a BHT of 175°C at 2949 mbgs and a geothermal gradient of 59°C/km (Arney et al., 1984). The MH-1 hole, drilled approximately 1.5 km to the east of MH-2 in 1986, had a BHT of 93°C at 1219 mbgs and a geothermal gradient of 69°C/km (Lewis and Stone, 1988). In addition to these heat flow and temperature data, a prominent regional Bouguer gravity anomaly (gravity high) extends through much of the WSRP (Figure 11). Shervais et al. (2002) interprets this anomaly to represent an uplifted horst block in the subsurface (Figure 6). The WSRP is bounded by high-angle normal faults dipping towards the axis of the SRP and contains interpreted intrabasinal antithetic normal faults (Shervais et al., 2002; Lewis and Stone, 1988). These antithetic faults are believed to have contributed to the uplift of the gravity anomaly-causing block. Fracture density is typically greater on the flanks of gravity anomalies due to fault-related uplift making them attractive areas for geothermal exploration. The MH-2 hole location was

chosen near the southwest edge of the gravity high near the interpreted intrabasinal faulted block because of potential for encountering thermal fluids associated with the structure and high permeabilities of faulted rocks.

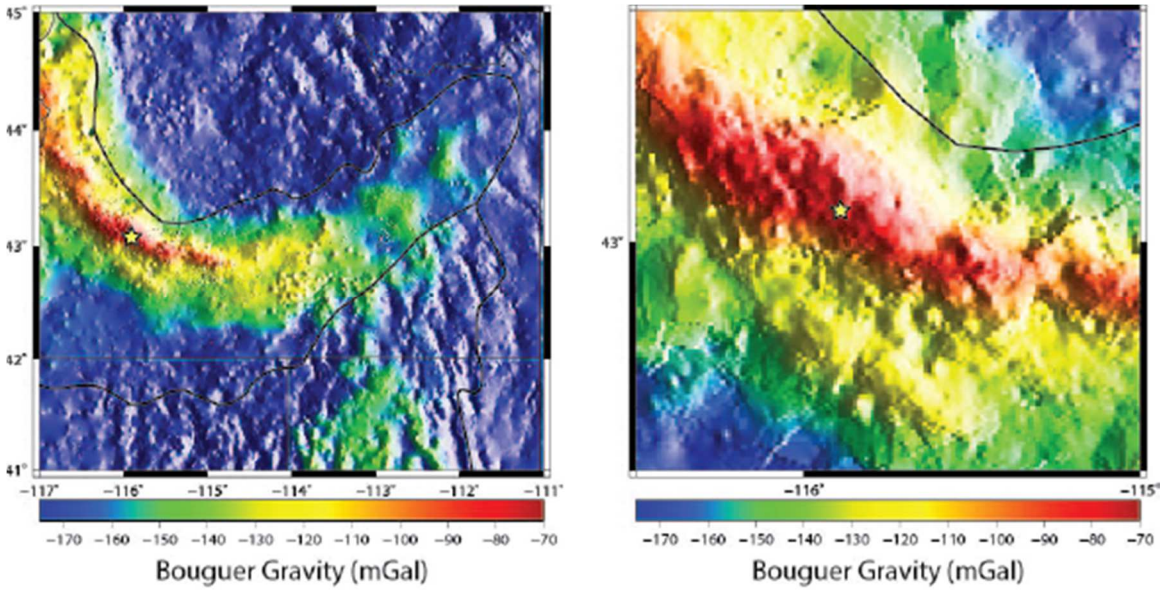

Figure 11: Gravity anomaly of the WSRP; Left: Regional Bouguer gravity map of the SRP; Right: Regional Bouguer gravity anomaly of the WSRP; Star denotes the location of the MH-2 and red indicates a positive anomaly while blue is negative.

MH-2 drilling was advanced to a total depth (TD) of 1821 mbgs and ended on January 31, 2012 (Shervais et al., 2014). The average geothermal gradient was ~73°C/km, the highest of all the Project Hotspot wells (Figure 12), but influx from shallow aquifers caused some fluctuations on the temperature log. At a depth of 1745 mbgs, geothermal fluids were encountered at a temperature of 150°C and flowed to the surface at a rate of 42 L/min. These fluids were sampled for geochemical analyses (Lachmar et al., 2012).

Basalt is the dominant rock type encountered in the MH-2 borehole (Figure 12). The upper basalts are massive with large phenocrysts of plagioclase. These range in age

from 100-900 ka based on dating of volcanic structures in the immediate vicinity of MH (Shervais and Vetter, 2009). At approximately 200 mbgs, lacustrine sandstones and mudstones, thought to have originated from the Lake Idaho, dominate to a depth of 750 mbgs. Basalt with minor intercalated sediment layers continues to a depth of 1200 mbgs. These basalts have been partially altered by hydrothermal activity and are recognized by slight oxidation and clay alteration. Below 1200 mbgs, a thick package of basalt flows, hyaloclastites (evidence of subaqueous eruption) and basaltic sandstones are present and tend to be altered green due to the presence of alteration clays. At approximately 1700 mbgs, light gray aphanitic to dark gray and black aphanitic, massive, olivine tholeiite basalt is dominant. These thick packages of basalts that underlie the Lake Idaho sedimentary deposits are dated to be approximately 9 Ma (Jenks and Bonnichsen, 1989, Wood and Clemens, 2002, White and Hart, 2002, Bonnichsen and Godchaux, 2002).

Large aperture fractures (10-15 mm) and vugs, along with hydrothermally brecciated basalts, are prevalent throughout this zone with some being completely or partially filled with secondary minerals. Mineralized fractures are abundant and are filled with calcite, disseminated quartz, and laumontite. Additional minerals found in core include pyrite, chalcopyrite, smectite, chlorite, and corrensite (Armstrong et al., 2013). At approximately 1740 mbgs, calcite and laumontite crystals are scattered on fractured surfaces and vugs but do not completely fill voids and fractures.

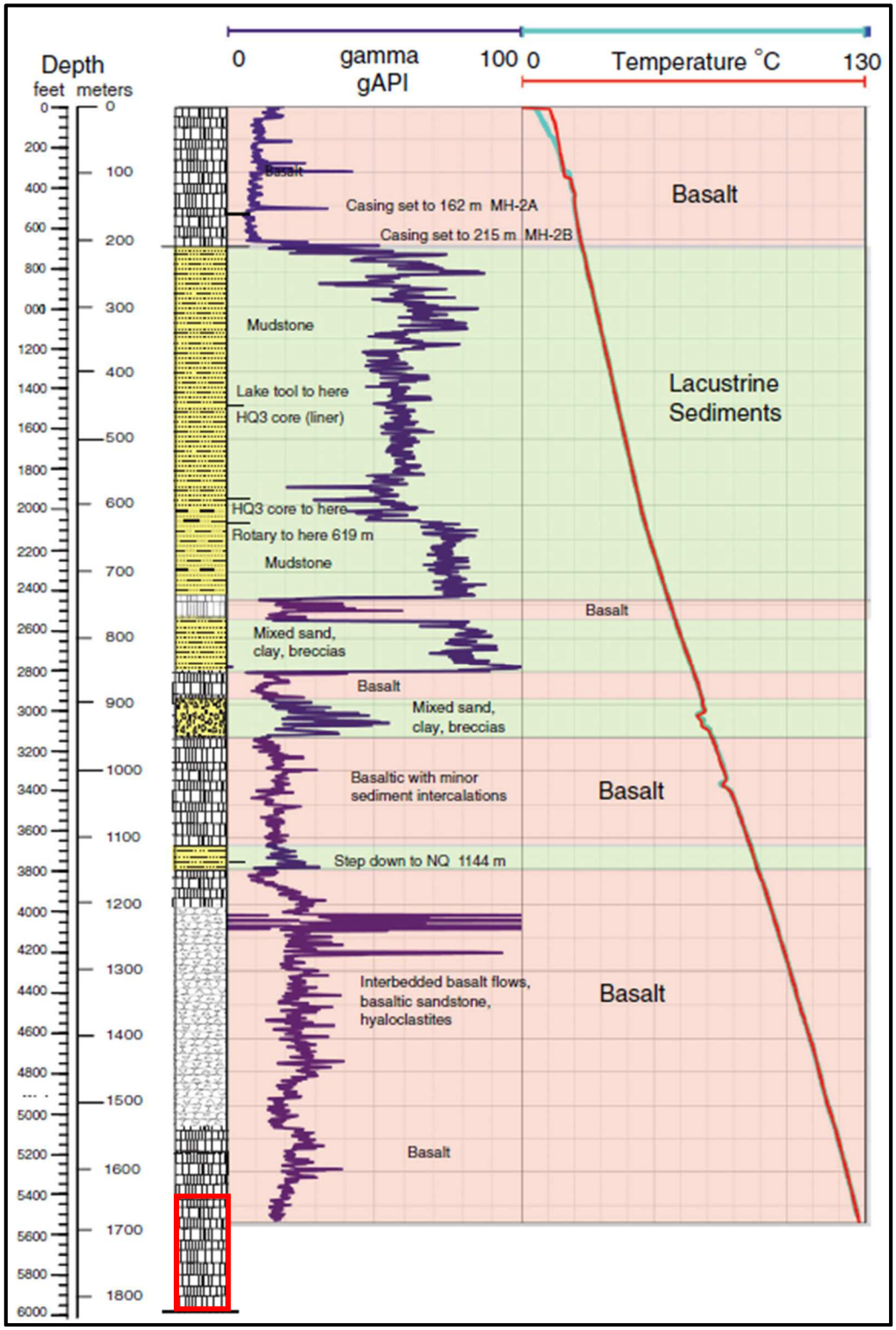

Figure 12: Lithology, gamma ray, and temperature logs of the MH-2 borehole with the ZOI for this study outlined in red; (modified from Shervais et al., 2013)

2.3.2 Core Fracture Analysis and Mechanical Properties

Kessler et al. (2014) performed high-resolution fracture and mechanical property analyses throughout a zone of interest (ZOI) from 1280-1821 mbgs in order to characterize the stress regime of the MH geothermal system. Data collected include: fracture density, cumulative fracture frequency, fracture orientation, and fracture aperture. These data were gathered from both core and the borehole acoustic televiewer data provided by Southwest Exploration.

Kessler identified two zones of the MH core that lacked detectable fractures at depth ranges of ~1349-1384 mbgs and ~1481-1532 mbgs (Figure 13). Most of the fracture apertures in the core were <10-15 mm wide. Zones of larger fractures and voids (20-113 mm) are inferred from lack of core recovery (<50%). High temperature secondary mineralization suggests potential high fluid flux in these fracture networks.

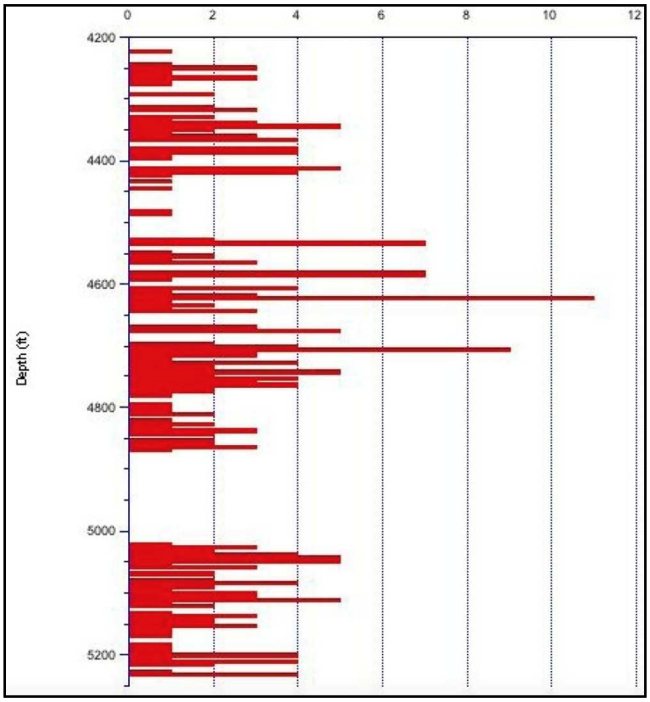

Figure 13: Fracture frequency distribution as a function of fracture density (# of fractures/5 ft of borehole depth); (modified from Kessler et al, 2014)

Dip directions of the fractures cluster in three directions: primary-NNW, secondary-SSE and tertiary-WSW. Although the dip angles (40-80°) are consistent with the regional high angle normal range-front faults, the orientation of the fractures vary from the regional structure. For example, the primary cluster of fractures has the same orientation as one set of Quaternary faults (NW-SE) in the area but the dip direction is antithetical (NE-SW) (Figure 5).

Kessler also performed mechanical analyses to gain better insight into the lithologic, elastic, and physical properties of the MH-2 core. Data gathered include: uniaxial compressive strength (UCS), static Young's modulus, static Poisson's ratio, dry bulk density, and pneumatic permeability. Correlation of these data with the fracture data revealed nine unique mechanical stratigraphic units (Figure 14). Kessler identified three units (2, 5, and 8) that exhibit ductile deformation with a lack of brittle failure during UCS experiments. Unit 1 is the host of the MH geothermal system and exhibits brittle failure when tested for UCS. Because of the stratigraphic relationships between Unit 1 and Unit 2, Kessler postulates that the weak, ductile Unit 2 may be acting as a seal to the system arresting the escape of geothermal fluids and heat found in Unit 1.

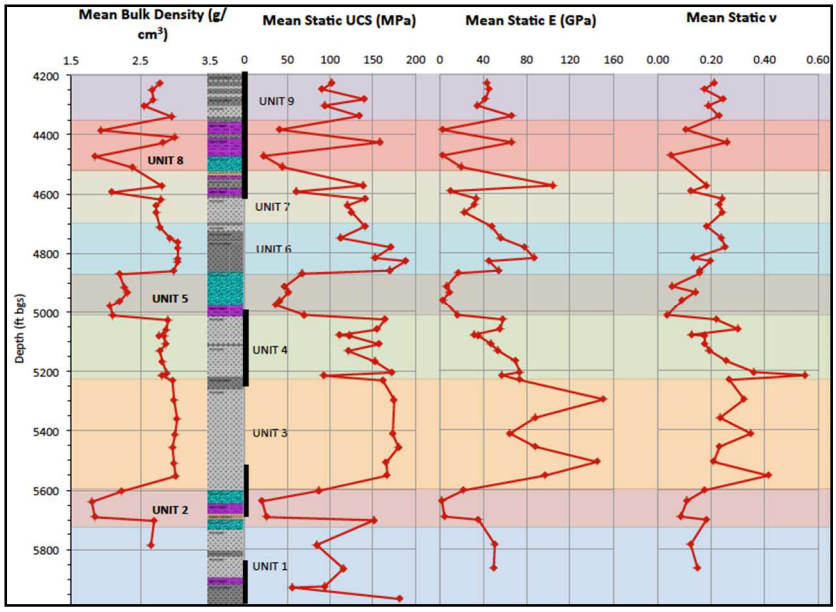

Figure 14: Mechanical stratigraphy of the MH-2 borehole; Note the weak Unit 2 containing altered and basalt breccias (purple and blue) overlying the stronger Unit 1 with crystalline basalts (light and dark gray). Fault/shear zones are indicated with black bars next to the lithology log. (modified from Kessler et al. 2014)

2.3.3 Clay Mineralogy

Wheeler (2013) sampled 23 areas of core from 720-1820 mbgs and performed detailed X-ray diffraction analysis on 10 of those samples from 1750-1820 mbgs. Three main clay minerals were identified based on XRD peaks: saponite (trioctahedral smectite), chlorite, and corrensite. These Mg alteration clays have been found in various settings including fractures in metamorphic basement in France (Beaufort and Meunier, 1994), hydrothermally altered basalts in California (Bettison and Mackinnon, 1997) and in geothermal systems of El Salvador (Roberson et al., 1999). In the MH-2 core, saponite dominates from 760-1750 mbgs and corrensite, a R1 (1:1) chlorite/smectite layered clay, dominates from 1750-1800 mbgs. Below 1800 mbgs, saponite again is dominant. Clay transitions from smectite-corrensite-smectite near the zone of artesian water suggests high temperature alteration above 150°C

2.3.4 Geothermal Fluid Analysis

On 26 January 2012, the drilling at MH encountered geothermal water at 1745 mbgs that flowed from artesian pressure to the surface where it was sampled and later analyzed. Field measurements were conducted including temperature, pH, electrical conductivity, salinity, and alkalinity after 12 hours of continuous flow. Analyses included major and trace elements, deuterium (δD_{SMOW}), oxygen isotope ratios ($\delta^{18}O_{SMOW}$), carbon isotope ratios ($\delta^{13}C_{PDB}$) of dissolved inorganic carbon (Table 1).

Table 1: Field measurements and major ion chemistry of geothermal waters from the MH-2 borehole. Unless otherwise stated, all values are in mg/L. Alkalinity reported as mg/L HCO_3^-. (modified from Lachmar et al., 2012, Freeman, 2013)

T (°C)		**Conductivity (µS)**			**pH**	**Salinity (ppt)**		**Alkalinity (mg/L)**	
31.3		870			9.59	0.4		100	
Ca	**Mg**	**Na**	**K**	**Alkalinity**	**Cl**	**SO_4**	**δD_{SMOW}**	**$\delta^{18}O_{SMOW}$**	**$\delta^{13}C_{PDB}$**
8.71	0.16	288	9.02	100	74.8	477	-88	-3.2	-10.87

A temperature of 150°C was measured with the DOSECC BHT tool at the depth of the large fracture zone and artesian flowing waters (Armstrong et al, 2013). Down-hole temperatures measured at 1355 mbgs (119 m above the fracture zone), were 135°C and subsequent down-hole logging revealed a BHT of ~135-140°C possibly as a result of downward flow of cold water (Nielson et al., 2012). The field measurement of 31.3°C is likely the result of dilution of geothermal fluids after the 12 hours of continuous flow. No other field measurements were made earlier to this period other than the BHT temperatures mentioned above.

The MH-2 waters indicate that it is a Na-SO_4/Cl^- type water (Figure 15). Lachmar et al., (2012) suggests that because of the high pH of 9.59 and relatively high sulfate levels, the water is in pH controlled by water-rock interaction with basalt at the

measured temperature and that the oxidation of pyrite in the core is most likely the main source of sulfate in the system. The δD_{SMOW} and $\delta^{18}O_{SMOW}$ values of -88 and -3.2 ‰, respectively, suggest that the water is a mixture of meteoric groundwaters that exchanged with silicates at high temperatures (Lachmar et al., 2012). The MH-1 waters measured from 610 mbgs had δD_{SMOW} and $\delta^{18}O_{SMOW}$ values of -126 and -14.6 ‰, respectively (Lewis and Stone, 1988). These waters are compared to other SRP and Yellowstone thermal waters (Figure 16). The relationship between MH-1, MH-2, and "magmatic waters" could suggest mixing of meteoric waters and waters from a relict geothermal system. The MH-2 waters could also represent water that has been shifted in $\delta^{18}O$ due to high temperature exchange with silicate bedrock similar to what has been documented in Iceland (Mutonga et al., 2010).

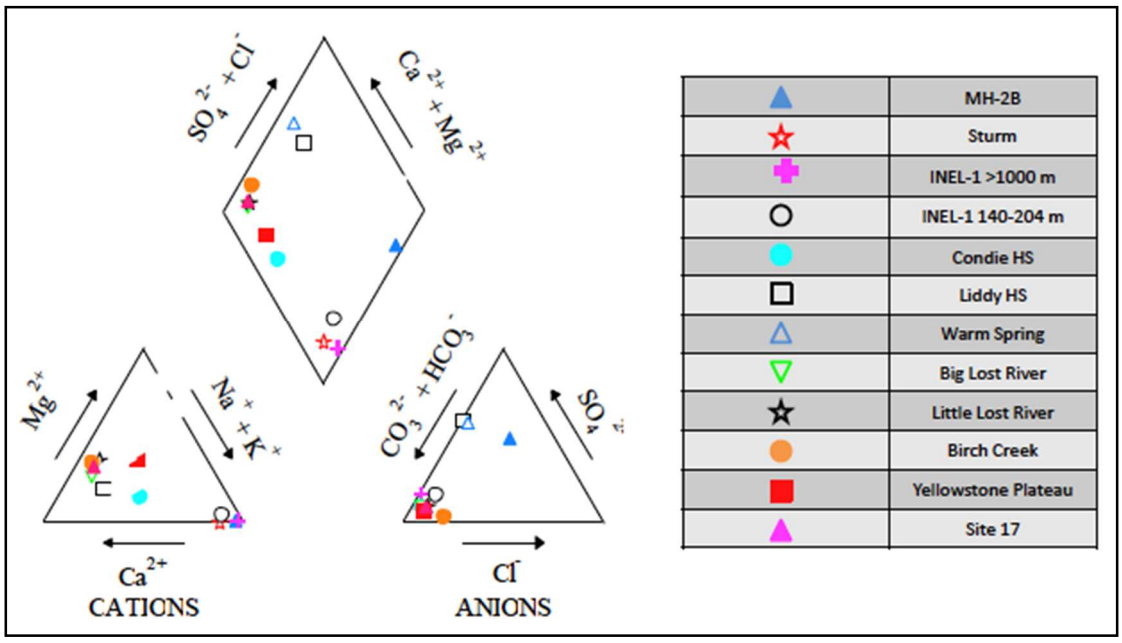

Figure 15: Piper plot of the geothermal water from the MH geothermal system compared to other SRP geothermal waters reported by McLing et al., 2002 (modified from Lachmar et al., 2012)

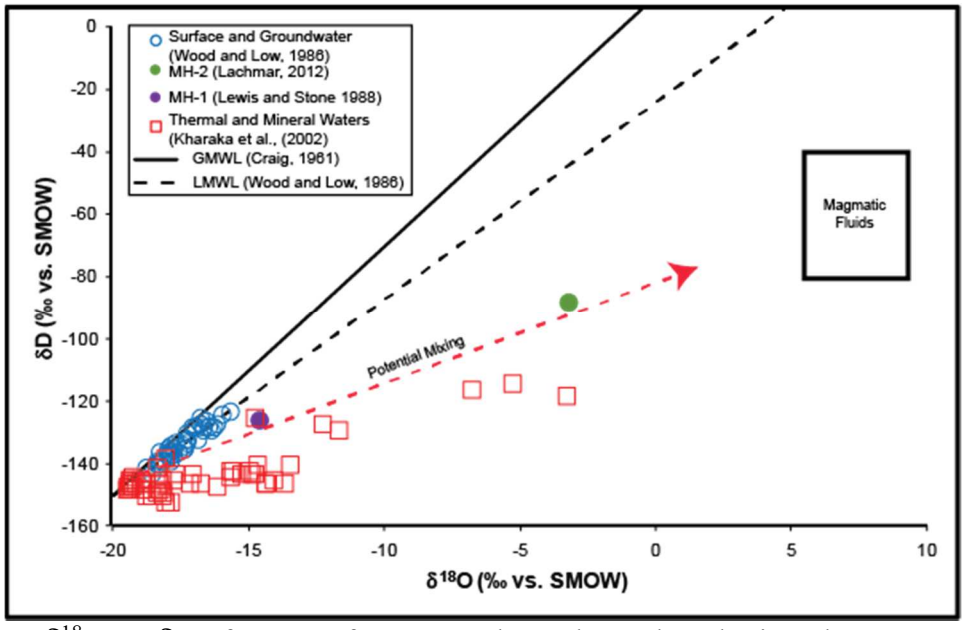

Figure 16: $\delta^{18}O$ vs. δD of SRP surface, ground, geothermal, and mineral waters; Note the deviations of the MH-1 and MH-2 waters from the GMWL.

Freeman (2013) applied chemical geothermometers to estimate reservoir temperatures at depth including quartz (Fournier and Potter, 1982), Na/K (Fournier, 1981), Na/K (Giggenbach, 1988, 1991), and Na-K-Ca (Fournier, 1973). The following assumptions are generally made when applying these equations: 1) the relevant hydrothermal minerals of the system are in equilibrium with geothermal fluids; 2) the reservoir pore-fluid pressure is fixed by liquid and steam coexistence; 3) cooling of the geothermal fluid occurs through conduction or adiabatically through steam separation at 100°C; 4) no mixing occurs with shallower cold water sources during rise of geothermal fluids; and 5) precipitation of minerals from the geothermal fluid does not occur along the upflow path (Ferguson et al., 2009). The calculated equilibrium temperatures of the MH-2 waters range from 132-154°C, similar to those of the present-day temperatures.

3. METHODS

3.1 SAMPLE COLLECTION

The ZOI of this study includes 172 m (1649-1821 mbgs) of massive and altered basalt, hyaloclastite, and basaltic sandstone. This area was targeted based on the high-density of mineralized fractures and its location relative to the artesian flowing zone. The goal was to create a high-density sample of compositions from observed mineralized veins in the core and make observations of host rock alteration. The minerals sampled for microscopic observation and laboratory analysis include secondary calcite, laumontite and an unknown white vein-filling mineral. The samples were collected by micro-drilling of veins, fracture-fill, vesicles, and voids using a Dremel 3000 Rotary Tool with a diamond coated bit. A total of 128 powdered carbonate samples were collected via this method for stable isotope analysis. Thirty four one-inch diameter plugs were drilled from the core using an 8" diamond drill bit mounted to a drill press. These were extracted between the same depth interval near zones with varying amounts of mineralization as well as basalt matrix with the intent of preparing thin and thick sections for spectroscopy and fluid inclusion microthermometry, respectively. Powdered sample and plugs were taken from the same depths in order to compare the mineralogical observations with the stable isotope and fluid inclusion measurements.

3.2 SAMPLE PREPARATION

3.2.1 X-ray Diffraction Samples

Rock chips were cut from the upper section of the ZOI (1652-1702 m) with a rock saw. These chips were crushed to flour consistency in a shatter box with a zirconium

dish. Samples were then loaded into a 2.5 cm long x 0.4 cm deep rectangular sample tray for analysis. The whole-rock powders were pressed by hand into the tray producing a mostly-random oriented powder.

3.2.2 Stable Isotope Samples

Powdered samples for carbonate stable isotope analysis were weighed out to 150-200 μg and placed in 12 ml EXETAINER® vials. Two international carbonate standards (NBS 18 and NBS 19) were placed at the beginning and end of each run for calibration to the PDB scale. Additionally, two in-house standards (Yule 80 and Yule 120) were placed randomly throughout each run to correct for linearity and drift of the mass spectrometer. To correct for linearity, samples of Yule 80 were measured from a range of 100-500 □g and to correct for drift, all samples of Yule 120 were measured out to approximately 150 μg. Samples were loaded into a 50°C reaction tray and flushed with ultra-high purity helium for 6 minutes. After flushing, 100 μl of anhydrous phosphoric acid was added to each sample and left to react at 50°C for two hours to allow for complete CO_2 release (McCrea, 1950).

3.2.3 Thin and Thick Sections

Fragile and friable plugs were impregnated and/or glued using EPOTEK 301 before billet preparation. Billets were then cut from the one inch plugs with a rock saw and sent to Spectrum Petrographics Inc. to be prepared as thin (30 μm) and thick sections (100 μm). Thirty one samples were prepared for thin section petrography and left uncovered for Scanning Electron Microscopy (SEM) and Electron Microprobe Analysis

(EMPA). Thin sections used for EMPA were carbon coated and polished again prior to analysis under high vacuum. Fifteen thick sections were made and doubly polished in order to perform fluid inclusion microthermometry. The prepared thick sections were removed from the glass slides by soaking in acetone overnight. Chips were then selected and fixed to a new glass slide with Krazy Glue in order for desired placement on the cooling/heating stage.

3.3 SAMPLE ANALYSIS

3.3.1 X-ray Diffraction Analysis

X-ray Diffraction analyses were carried out at Utah State University using a Philips PANalytical X'Pert X-Ray Diffractometer (XRD). The raw data were collected using PANalytical X'Pert Data Collector, version 2.0b, published February 27, 2003, and the interpretations of the data were done using PANalytical X'Pert HighScore version 2.2.0, published January 2, 2006. All scans were run using CuKα radiation at 45 kV and 40mA.

3.3.2 Stable Isotope Analysis

Analyses of carbon and oxygen stable isotope ratios in carbonate were accomplished in the Department of Geology Stable Isotope Laboratory at Utah State University using a Thermo Delta V Advantage Isotope Ratio Mass Spectrometer and a GasBench II with a PAL auto-sampler. The software used to gather stable isotope data is ISODAT 3.0 Gas Isotope Ratio MS Software©. The carbonate-phosphoric acid digestion method (Equation 2) was utilized to liberate CO_2 from the carbonates (McCrea, 1950).

$$3CaCO_3 + 2H_3PO_4 \rightarrow 3CO_2 + 3H_2O + Ca_3(PO_4)_2. \quad (2)$$

The generated gas was passed to the gas-bench with a He carrier gas for purification and gas separation and transferred to the mass spectrometer for measurement. Isotope ratios were determined using measurements of mass 44, 45, and 46 relative to the in-house reference CO_2 gas. Linear regressions were made in MS Excel® to correct for linearity and drift throughout the runs. Calibration to the PDB scale was also accomplished by performing a linear regression using the internationally agreed value of the NBS standards and the measured standards relative to the in-house reference CO_2. All results are on the PDB (Pee Dee Belemnite) scale, reported in delta (δ) notation. Values are in per mil (‰) calculated by equations 3 and 4 with 0.07 ‰ error in $\delta^{13}C$ and 0.08 ‰ error in $\delta^{18}O$ calculated as an average of the standard deviations of replicate measurements of the in-house standards.

$$\delta^{13}C_{\text{sample PDB}} = \frac{\frac{13}{12}C_{\text{sample}} - \frac{13}{12}C_{\text{standard PDB}}}{\frac{13}{12}C_{\text{standard PDB}}} * 1000 \quad (3)$$

$$\delta^{18}O_{\text{sample PDB}} = \frac{\frac{18}{16}O_{\text{sample}} - \frac{18}{16}O_{\text{standard PDB}}}{\frac{18}{16}O_{\text{standard PDB}}} * 1000 \quad (4)$$

All results on the SMOW (Standard Mean Ocean Water) scale, are reported in delta (δ) notation and values in per mil (‰) calculated by equation 5. The O isotope values were converted to the SMOW scale for use in geothermometry calculations.

$$\delta^{18}O_{\text{sample SMOW}} = 1.03091 * \delta^{18}O_{\text{sample PDB}} + 30.91 \quad (5)$$

3.3.3 Thin Section Petrography

All thin section petrographic observations were made using a Leica DM 2700P petrographic microscope equipped with a Leica MC 170 HD camera. Whole section photos were taken using the camera mentioned above but on a Leica Z16 APO microscope. Leica Application Suite 4.6 software was used to capture digital photos.

3.3.4 Fluid Inclusion Microthermometry

Fluid inclusions of calcite samples were analyzed in the Department of Geology at Utah State University using a Fluid Inc. adapted USGS gas-flow heating-freezing system. A full calibration was performed using a synthetic pure H_2O inclusion (positive span) and a synthetic 25 mol % CO_2-H_2O inclusion (negative span). The calibration procedure that was utilized can be found in Mazurek, 2004. The synthetic fluid inclusion standards were obtained from the Fluid Inclusion Laboratory Leoben in Austria. A Zeiss Universal transmitted-light research microscope equipped with a Zeiss Epiplan 50x long-working distance objective and Canon Powershot G7 10MP digital camera were used for observing the behavior of the inclusions at various temperatures. The 100 μm sections of the MH-2 core were placed in the metal housing of the stage and heated to the temperature of homogenization (T_h). They were also frozen to measure the temperature of melting (T_m) in order to gain insight into paleo-composition of the precipitating fluids. Repeat measurements (n=5) on T_h and the T_m ice were measured in calcite samples according to the cycling procedures described in Goldstein and Reynolds, (1994) (Figure 17) and are accurate to within +/- 3-5°C.

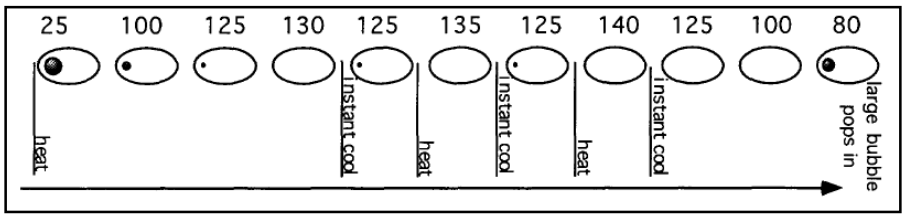

Figure 17: The cycling procedure to measure T_h; Ovals are two phase fluid inclusions. The numbers above are hypothetical temperatures in °C and the arrow indicates the progression of time. This diagram shows a T_h somewhere in between 135 and 140°C because the inclusion had to be undercooled 80°C before re-nucleation occurred. (modified from Goldstein and Reynolds, 1994)

Past hydrothermal fluid temperatures are estimated using pressure corrected T_h measurements. Isochores assuming both a lithostatic and hydrostatic pressure scenario were calculated using the geochemical bulk fluid modeling software FLUIDS v.1.0 (Bakker, 2003). The lithostatic and hydrostatic loads on the system (Equations 6 and 7) were estimated by

$$P_{lith}=\rho_{lith}gz \qquad (6)$$

$$P_{hydro}=\rho_{hydro}gz \qquad (7)$$

where P is the pressure at a given depth z (mbgs), ρ is the rock or fluid density, and g is the acceleration due to gravity (9.81 m/s^2). The following assumptions were used in estimating rock and fluid density:

- ρ basalt=2800 kg/m^3
- ρ lake sediments=2200 kg/m^3
- ρ water=1000 kg/m^3 (this assumes the fluid salinity does not significantly increase density)

The lithological log was used to estimate the proportion of basalt (70%) and sediment (30%) contributing to an estimated dry bulk rock density of 2620 kg/m^3. Salinity and fluid density of each inclusion were inputted into FLUIDS and by using the

equations of state (Bodnar and Vityk, 1994, Knight and Bodnar, 1989), the program output fluid isochores of each sample. These isochores were then linearly regressed to calculate T_t using both lithostatic and hydrostatic pressure at the depth of each inclusion.

3.3.5 Electron Microprobe Analysis

Uncovered, carbon coated thin sections were analyzed in the Electron Microprobe Laboratory at Brigham Young University using a Cameca SX50 Electron Microprobe. Two samples were analyzed for 1) identification of the hard, non-calcareous, white veins found in the upper section of the ZOI and 2) compositional variations in the calcite veins near the artesian flowing zone. For the white veins the probe was set to 15KV acceleration voltage and 10nA beam current and a 10 μm beam size. For the calcite 15KV acceleration voltage was used with a 6 nA beam current and a 20 μm beam size so as to not cause pitting in the calcite. The various standards used to calibrate for the non-calcareous veins are as follows: Na–jadeite, Mg-San Carlos olivine, Al–anorthite, Si–wollastonite, K–orthoclase, Ca-Kakanui amphibole, Ti-sphene, Mn–spessartine, and Fe–grunierite. The various standards used for carbonate calibration are: Mg-dolomite, Ca-calcite, Mn-spessartine, Fe-siderite, and Sr-strontianite.

4. RESULTS

The objectives of this study are to 1) characterize the thermal evolution of the Mountain Home geothermal system by studying past temperatures and comparing them to those of today and 2) to quantify isotopic and compositional variations of paleo-fluids responsible for mineralization in the MH-2 core. These objectives were addressed by the collection and analysis of six datasets including: a physical description of the MH-2 core throughout the ZOI between 1650-1821 mbgs, thin section microscopic observations, X-ray diffraction results of the upper section mineralogy, electron microprobe analysis (EMPA) results of secondary minerals, carbon and oxygen stable isotope ratios in calcite mineralization, and fluid inclusion microthermometry measurements in calcite. These data sets test the hypothesis that the mineralization in the core was produced by past high-temperature hydrothermal activity related to magmatism.

4.1 PHYSICAL DESCRIPTION OF THE ZOI MINERALIZATION

The zone of interest (ZOI) that exhibits the highest degree of secondary mineralization extends from 1649-1821 mbgs (Figure 18) in the lowest section of MH-2 core. Scattered and localized hard white veins (identified as prehnite and pectolite, see section 4.4) (Figure 19a-c), and minor amounts of disseminated and vein-fill quartz are located from 1651-1703 mbgs. These veins are 0.5-2 mm wide and often combine to form veins >5 mm wide. These banded fractures are examples of classic hydrothermal system vein mineralization and have been documented in geothermal systems such as Cerro Prieto, Mexico (Bird et al., 1984) Pauzhetsk, Kamchatka (Naboko, 1970), New

Zealand Volcanic Zone (Browne and Ellis, 1970), and Nesjavellir, Iceland (Sigvaldason, 1963).

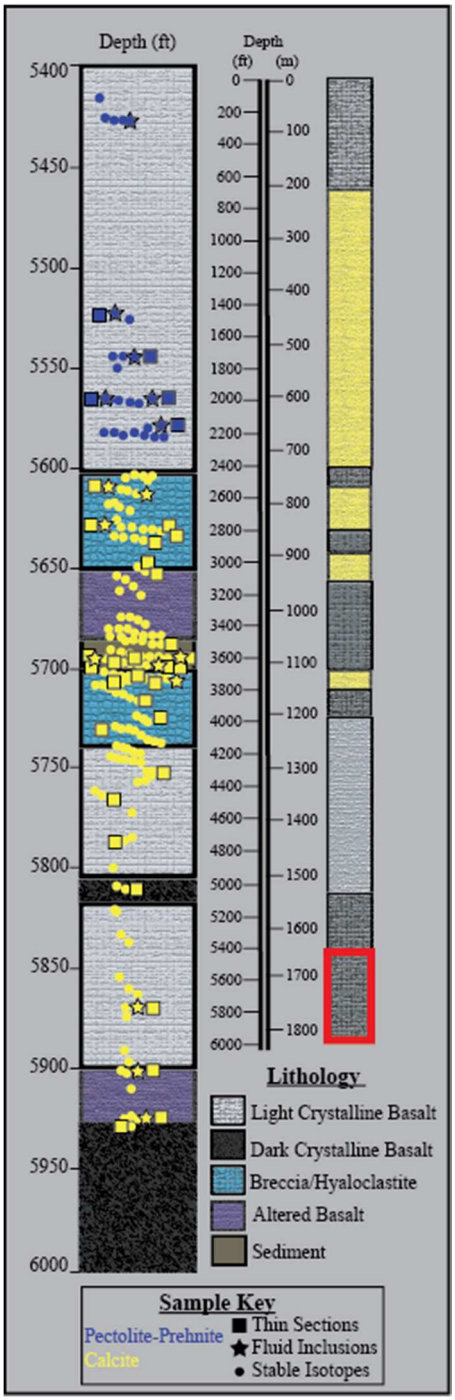

Figure 18: Lithology logs; The ZOI (red box) is from ~1646-1829 mbgs. Horizontal distribution represents areas of high-density sampling. (right-modified from Shervais et al., (2013); left-modified from Kessler et al., (2014))

Calcite mineralization extends from 1709-1809 mbgs beginning below a distinct lithologic contact at 1707 mbgs (Figure 21), where there is a transition from massive, dark gray, dense basalt lacking significant veins to a massive light gray, less dense, basalt with plentiful veins filled with calcite. This mineralization occurs in the form of fracture fill veins (Figure 19d-e and 20a), amygdules (Figure 19f), and euhedral calcite crystals that fill vugs and/or have been shaken loose during core handling (Figure 20b-d). Primary basalt breccias are common throughout this zone and are interpreted to have formed by hydrothermal activity (Nielsen and Shervais, 2014). These hydrothermal breccias include fragments of basalt trapped within a matrix of calcite (Figure 19d-e). Some fragments are altered to the same degree as the host rock but others include less altered massive basalt fragments that appear to have originated in a separate part of the system (Figure 22).

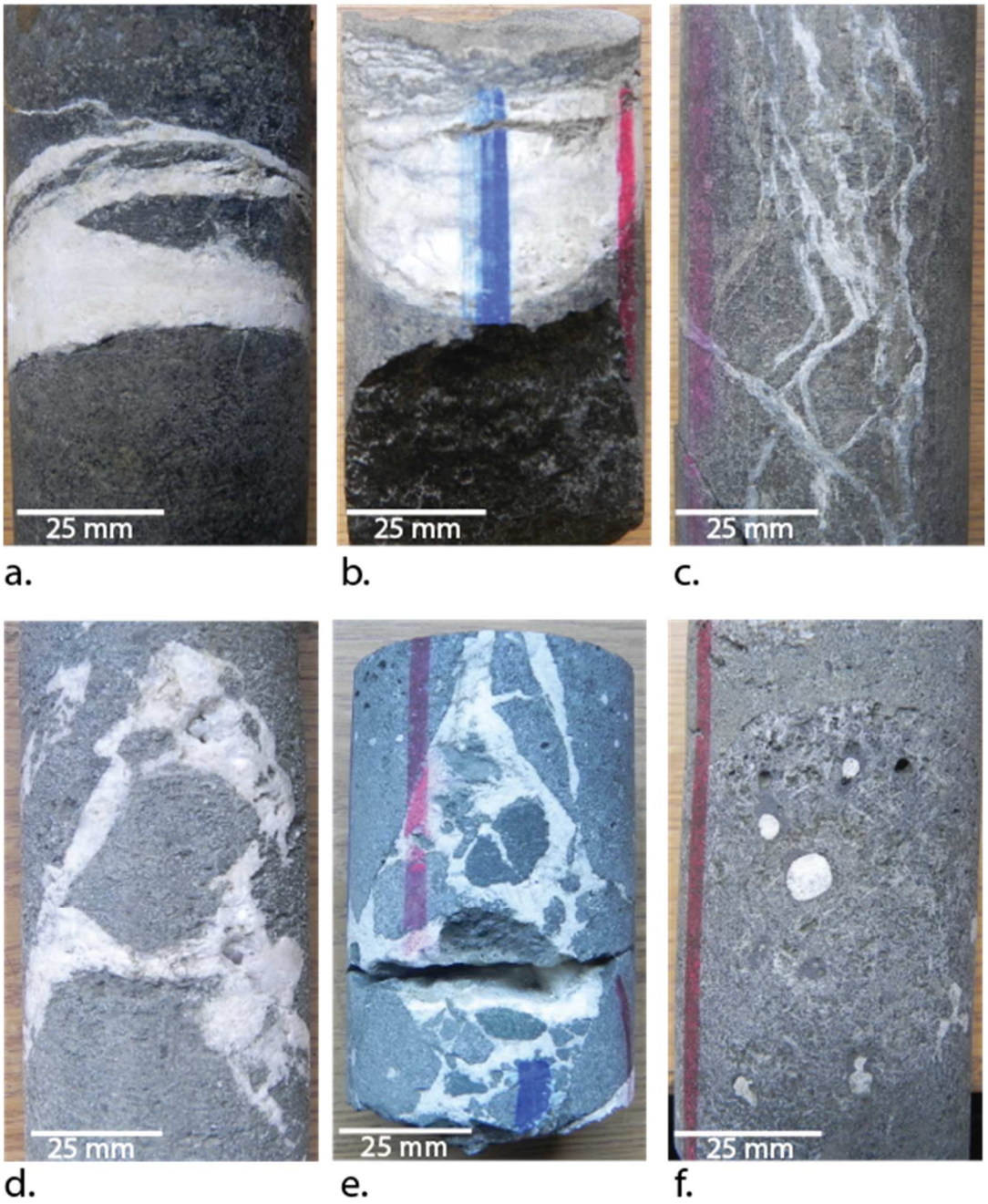

Figure 19: Images of the MH-2 core and mineralization; a-c: MH-2 core at 1690, 1652, 1684 mbgs (left to right) with white mineralized fractures containing prehnite and pectolite; d-e: Secondary calcite filling in between brecciated basalt fragments; f: Altered basalt with amygdule filled calcite from 1722 mbgs; Core is 5 cm (2 in.) in diameter.

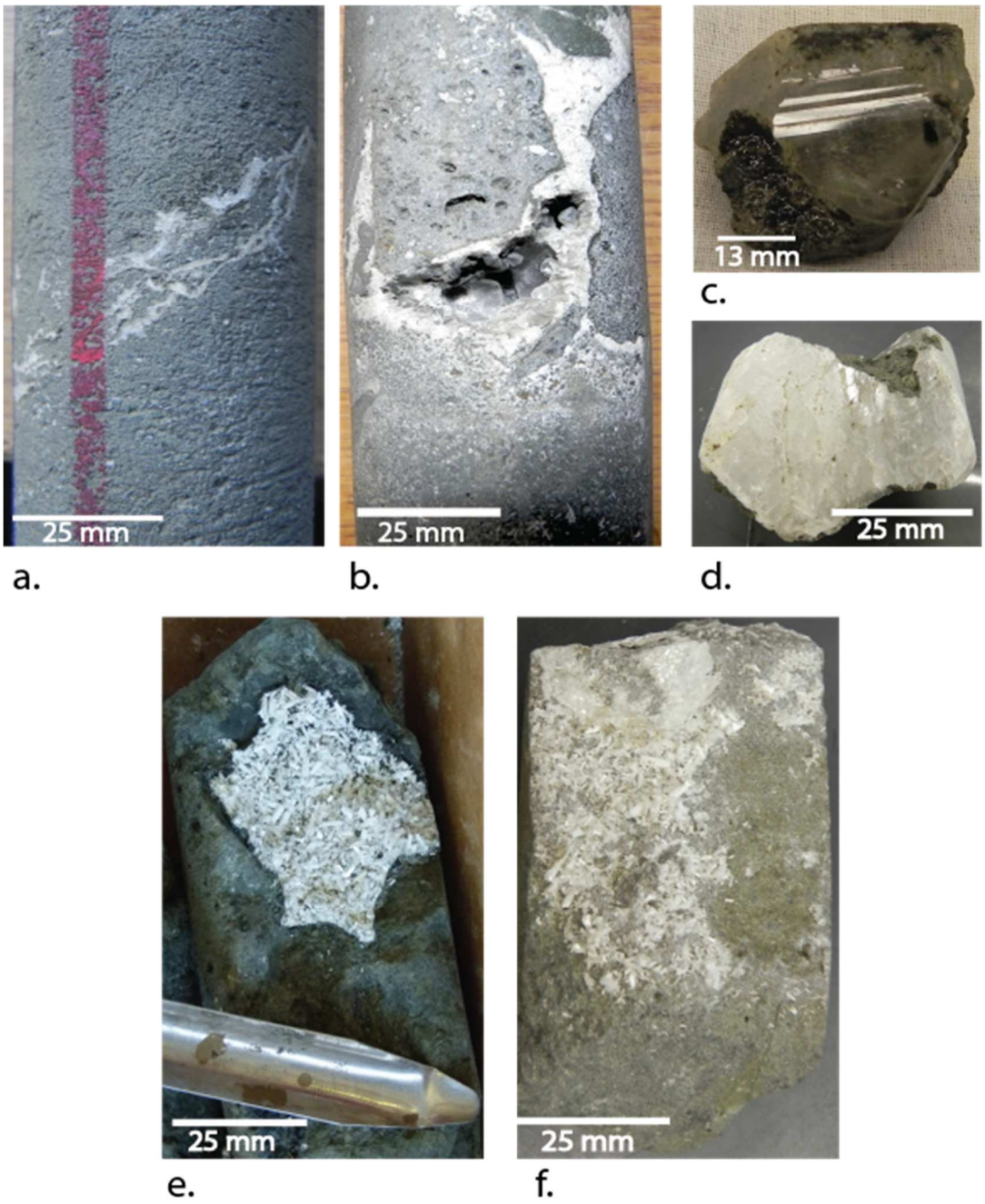

Figure 20: Images of the MH-2 core and mineralization a: Altered basalt from 1715 mbgs with calcite veins; b: Core from 1736 mbgs with euhedral calcite vug infilling; c-d: Loose 25 and 50 mm diameter euhedral calcite crystals from ~1789 and 1799 mbgs, respectively; e-f: Altered basalt from 1802 and 1756 mbgs exhibiting laumontite and calcite/laumontite mineralization, respectively.

At approximately 1740 mbgs, euhedral prismatic white crystals of laumontite are abundant and often present on fractured surfaces on top of calcite (Figure 20e-f). Loose laumontite and calcite crystals in core boxes are plentiful and scattered throughout the core to approximately 1800 mbgs. Calcite, although less abundant, becomes the dominant secondary mineral until TD.

Figure 21: Image of a MH-2 core box from 1707-1709 mbgs; Red arrow indicating the distinct lithologic contact between basalts hosting zones of prehnite and pectolite from basalts hosting calcite. Core deepens from right to left and top to bottom.

Figure 22: Image of diamictic breccia from 1734 mbgs in the MH-2 core; Note the difference between the rock type of the fragments surrounded by calcite (top portion) and the host basalt (bottom portion).

4.2 THIN SECTION PETROGRAPHY

Almost all the sections analyzed in this study contained varying amounts of hyaloclastite, as revealed by the presence of altered basaltic glass (sideromelane) that displays secondary alteration in the form of palagonite or clay alteration rims coating partially devitrified glass (Figure 23b). These rinds of palagonite form by surface interaction of mafic glass and aqueous fluids as the effusing lava comes into contact with water and subsequent devitrification (Stroncik and Schmincke, 2002). The clinopyroxene and olivine contents are low (<10%) and those crystals that are present display varying amounts of alteration, most likely to serpentine minerals, chlorite, and oxides. Most samples of relatively pristine, unaltered basalt, or basalt fragments, contain ~75% plagioclase. The following petrographic results are separated into 5 units based on secondary mineral presence and distribution: unit 1 (1652-1702 mbgs), unit 2 (1709-1730 mbgs), unit 3 (1732-1734 mbgs), unit 4 (1734-1800 mbgs), and unit 5 (1800-1807 mbgs).

Unit 1 is characterized by altered basaltic glass with secondary prehnite and pectolite veins that were identified in thin section by the bow-tie textures (prehnite) and low-middle 2nd order birefringence (pectolite) in cross-polarized light (Figure 23a) (Nesse, 2003). This is confirmed by subsequent X-ray diffraction and electron microprobe analyses (sections 4.3-4.4). Mineral grain sizes range from sub-millimeter to 4 mm in length. The finer-grained prehnite is located near the edges of veins, and the coarser-grained pectolite is observed filling the center of the veins (Figure 24e).

Unit 2 is defined by homogenous calcite veins that cross-cut altered basalt and the absence of pectolite and prehnite. This basalt is dominated by altered glass with

concentric rinds of palagonite (Figure 23b) and minor amounts (<5%) of plagioclase and pyroxenes. The calcite is characterized by interlocking grains approximately ~1-4 mm in the widest dimension. This calcite typically contains fragments of crystalline basalt and/or basaltic glass with the glass-calcite interface being quenched with the presence of fine-grained palagonite along the edges ~1 μm thick (Figure 23c).

Unit 3 (1732-1734 mbgs) is distinguished by the presence of microcrystalline quartz in addition to the palagonite–rimmed altered glass and calcite assemblage. The microcrystalline quartz cuts the calcite veins and incorporates laths of calcite within a microcrystalline quartz matrix (Figure 23d). Optical continuity is observed between the quartz and calcite indicating that calcite precipitation was followed by partial calcite dissolution and subsequent precipitation of quartz in the areas once occupied by calcite (Figure 23d). Quartz also appears as amygdule infilling of altered glass (Figure 23e) with palagonite rims.

Unit 4 is defined by less microcrystalline quartz and an increase of typical basalt minerals such as plagioclase, altered clinopyroxene, and Fe-oxides (Figure 23f). Although the Fe-oxides mostly seem to be primary, some cross cut plagioclase and pyroxenes and fill micro-fractures (Figure 24a). Secondary minerals include calcite, pyrite, and laumontite. Calcite is the dominant vein mineral and is also found in amygdules in the altered glass matrix (Figures 24b-c). Microcrystalline quartz is sparse throughout this section and cross cuts calcite and palagonite. Laumontite is present as abundant yet small crystals scattered on the core surfaces.

Unit 5 (1800-1807 mbgs) is characterized by more abundant calcite and microcrystalline quartz than found in unit 4. Relative abundances of primary Fe-oxide and clinopyroxene are lower that unit 4. The microcrystalline quartz fills small fractures cross-cutting the calcite (Figure 24d).

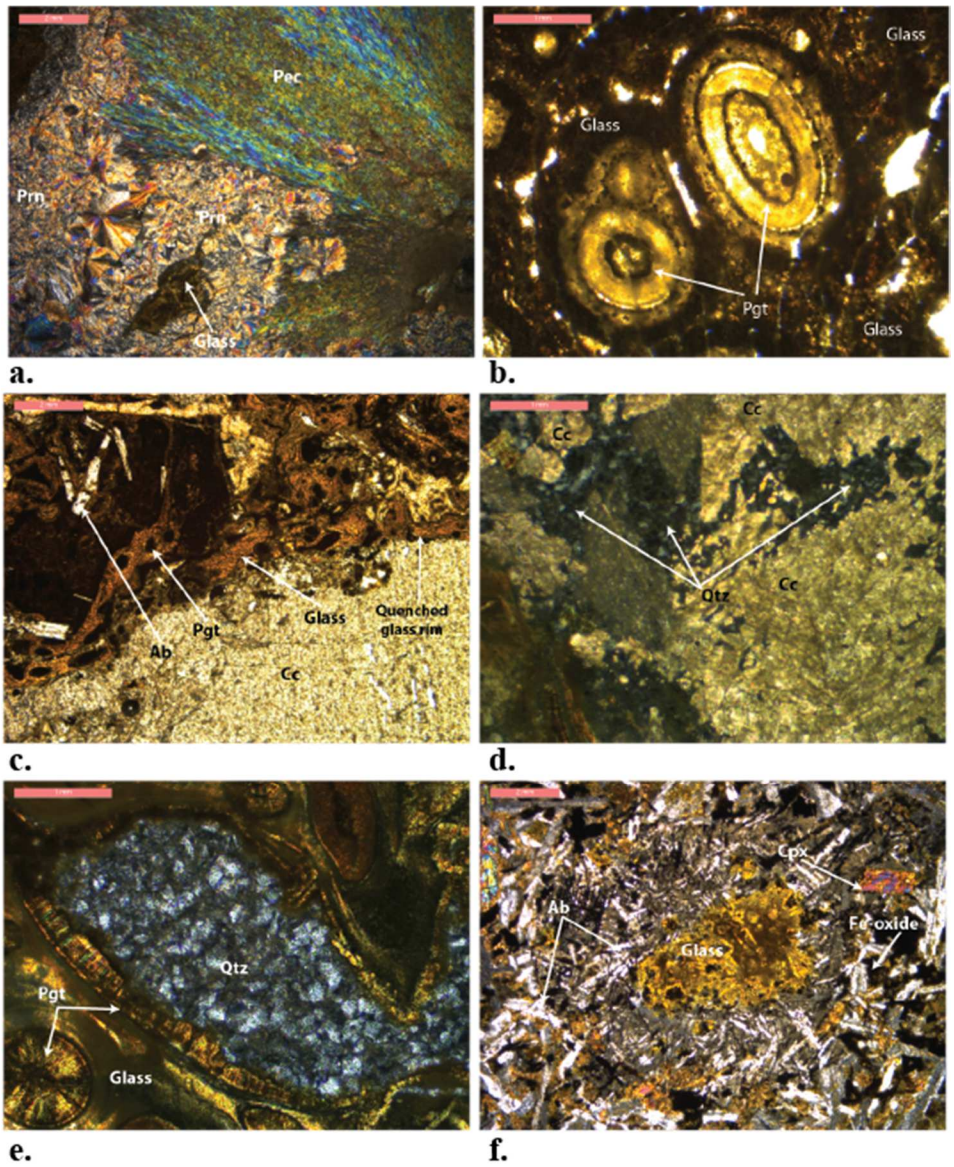

Figure 23: Photomicrographs of MH-2 core minerals; a. Prehnite (Prn) and pectolite (Pec) vein minerals from 1684 mbgs; Note the classic bow-tie structure in the prehnite, radiating habit, and 2nd order birefringence of the pectolite. b. Altered glass (siderlomane) with concentric rings of palagonite (Pgt) from 1709 mbgs; c. Altered glass, calcite (Cc), albite (Ab), and palagonite (Pgt) from 1716 mbgs; Note the quenched calcite-glass interface with fine-grained palagonite. d. Quartz (Qtz) and calcite (Cc) from 1734 mbgs; Note how the quartz cuts into the calcite and incorporates small laths of calcite within the quartz matrix. e. Quartz-filled amygdule with a palagonite (Pgt) rim, and glass matrix, from 1734 mbgs; f. Typical basalt albite (Ab), clinopyroxene (Cpx), glass, Fe-oxides from 1748 mbgs;

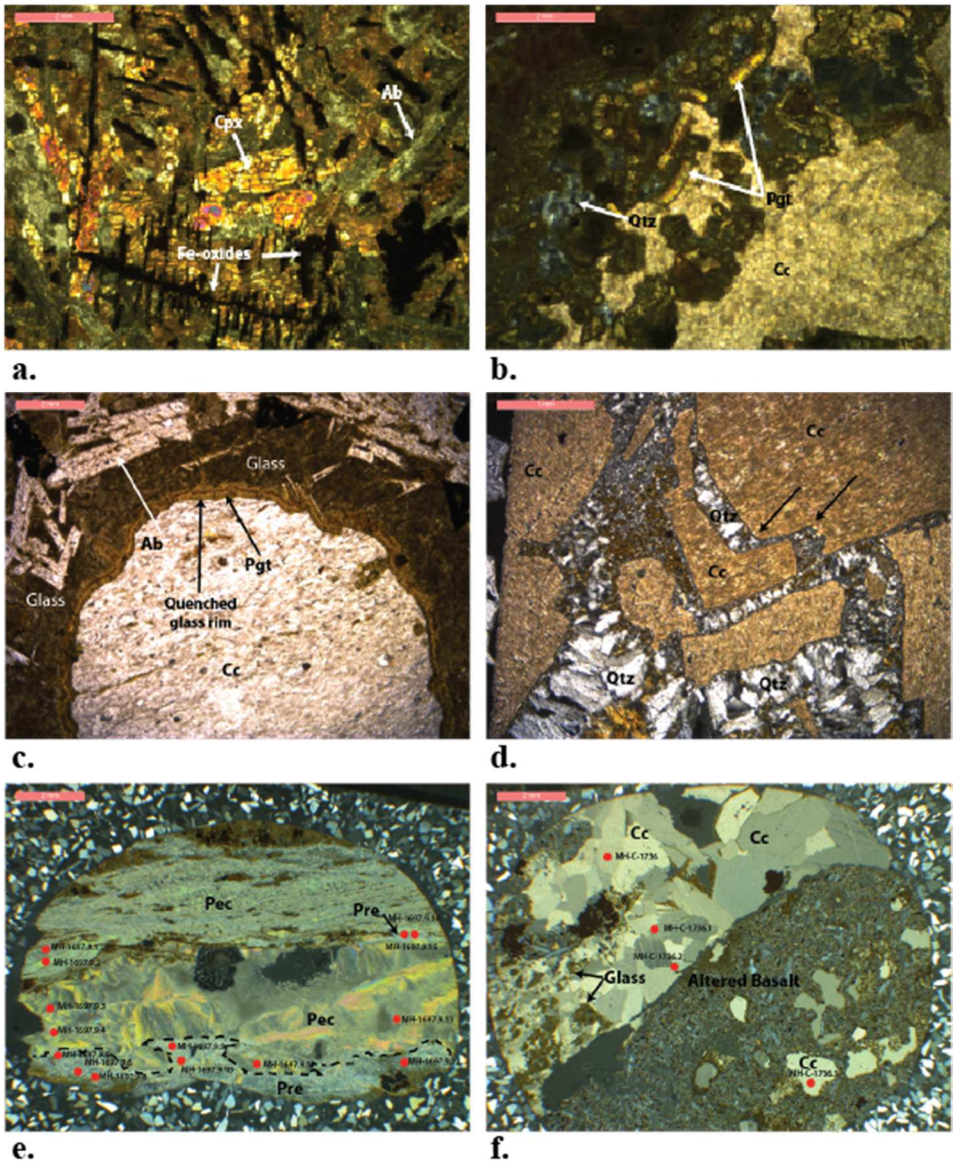

Figure 24: Photomicrographs of MH-2 core minerals a. Albite (Ab), clinopyroxene (Cpx), glass, and Fe-oxide from 1737 mbgs; b. Complex relationship between palagonite (Pgt) rinds, calcite (Cc), and quartz (Qtz) from 1738 mbgs; c. Amygdule fill of calcite (Cc) with palagonite (Pgt) rim from 1745 mbgs; d. Calcite and quartz from 1806 mbgs; Note the relationship between quartz and calcite. The angular piece of calcite in the center seems to have been cut at a ~90° angle by quartz (black arrows) due to the apparent displacement to the left and quartz infilling; e. EMPA results from MH-Q-1697.9 displaying the textural variability of a pectolite (Pec) and prehnite (Pre) vein; Pectolite is the main vein mineral located in the center and top parts of the vein. Prehnite is located on the edges of the vein next to the host rock (bottom) with sparse fragments scattered in the top portion of the photo. Red dots indicate approximate EMPA scan locations; f. EMPA results from MH-C-1736 analyzed for compositional variation throughout the calcite (Cc) vein; Red dots=scan locations.

4.3 X-RAY DIFFRACTION ANALYSIS

X-ray Diffraction (XRD) analysis was performed on four samples of the hard, white, non-calcareous veins in order to identify the secondary mineralization of the upper section (~1652-1702 mbgs) of the ZOI. These XRD results suggested that the vein minerals are prehnite ($Ca_2Al_2Si_3O_{10}(OH)_2$) and pectolite ($NaCa_2Si_3O_8(OH)$) (Figure 25). Uncertainty in these minerals required the further Electron Microprobe analysis (section 4.4) White prismatic crystals from the deeper sections of the core were collected and analyzed to verify the laumontite diffraction pattern (Figure 26) that had been identified previously (Armstrong et al., 2013) in order to compare to the patterns of the prehnite and pectolite.

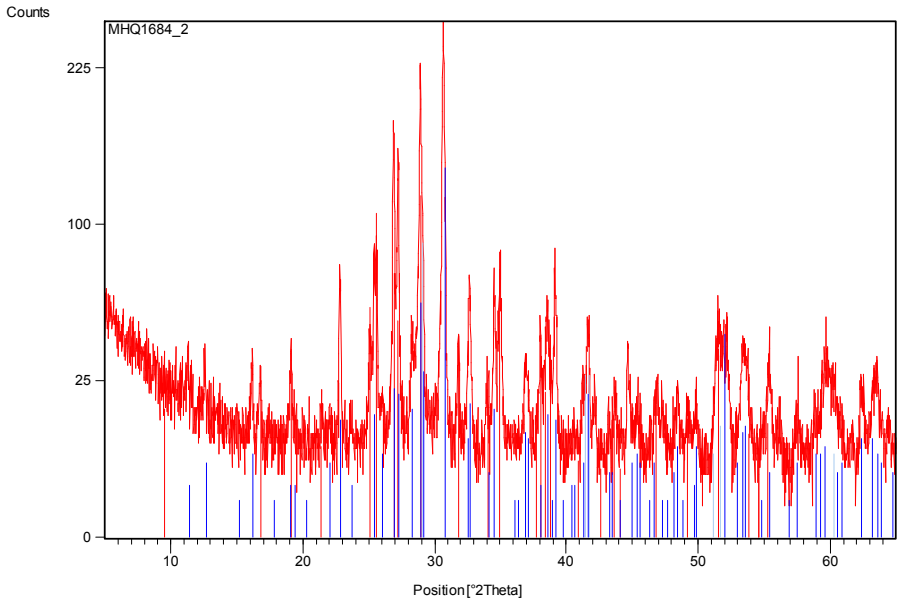

Figure 25: X-ray diffraction pattern of MH-2 core whole rock powders from 1684 mbgs; The peaks correlate with the mineral phases prehnite (red) and pectolite (blue).

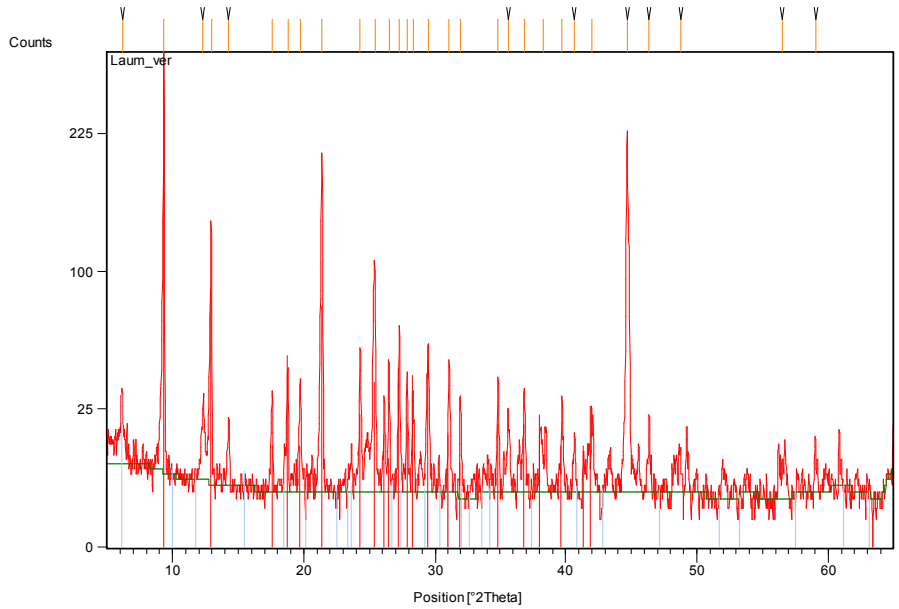

Figure 26: X-ray diffraction pattern from laumontite crystals gathered from various depths through the deeper section of core where laumontite had been previously identified (Armstrong et al., 2013)

4.4 ELECTRON MICROPROBE ANALYSIS

To confirm the existence of prehnite and pectolite that was identified by XRD, electron microprobe analysis was conducted on the white, non-calcareous vein material in unit 1 (Figure 24e, Tables 2 and 3). Oxide wt% values are consistent with those reported by Deer, Howie, and Zussman (2013) with <100% totals resulting from the semi-rough nature of the microprobe mounts and the omission of OH from the analysis. Scan I.D.'s 1697.9.1 through 1697.9.4 display 8.6-9.2 wt% Na_2O and 0.3-0.5 wt% Al_2O_3 indicating a composition consistent with pectolite. Scan I.D.'s 1697.9.5 through 1697.9.10 indicate less Na_2O (0-0.1 wt%), SiO_2 (42.0-47.4 wt%), and CaO (25.9-27.8 wt%) content with high Al_2O_3 (19.1-22.9 wt%) consistent with prehnite. EDS spectra of pectolite and prehnite confirm the EMPA results (Figure 27 and 28, respectively).

Table 2: EMPA of pectolite on sample 1697.9 (wt% oxide); Nominal water content of 3.0 wt% taken from Deer, Howie and Zussman (2013). Formula based on 9 oxygens. Elemental values are calculated atomic formula units (i.e. cations per formula unit).

Scan #	1697.9.13	1697.9.1	1697.9.2	1697.9.11	1697.9.4	1697.9.3
SiO_2	52.87	53.90	54.92	53.94	53.40	53.46
Al_2O_3	0.41	0.55	0.38	0.83	0.41	0.32
CaO	32.16	32.98	33.00	33.29	33.48	33.62
Na_2O	9.29	9.16	9.13	7.98	8.58	8.63
K_2O	0.00	0.01	0.01	0.02	0.01	0.01
TiO_2	0.00	0.00	0.00	0.00	0.00	0.00
MgO	0.00	0.00	0.00	0.00	0.00	0.00
FeO	0.11	0.08	0.08	0.06	0.01	0.10
MnO	0.11	0.38	0.27	0.27	0.24	0.28
$[H_2O]$	9	9	9	9	9	9
Total	97.95	100.05	100.80	99.38	99.13	99.41
Si	2.97	2.97	3.00	2.98	2.97	2.97
Al	0.03	0.04	0.02	0.05	0.03	0.02
Ca	1.94	1.95	1.93	1.97	1.99	2.00
Na	1.01	0.98	0.97	0.85	0.93	0.93
K	0.00	0.00	0.00	0.00	0.00	0.00
Mg	0.00	0.00	0.00	0.00	0.00	0.00
Fe	0.01	0.00	0.00	0.00	0.00	0.00
Mn	0.01	0.02	0.01	0.01	0.01	0.01
H	1.13	1.10	1.09	1.11	1.11	1.11
Sum	**7.08**	**7.05**	**7.02**	**6.98**	**7.04**	**7.04**

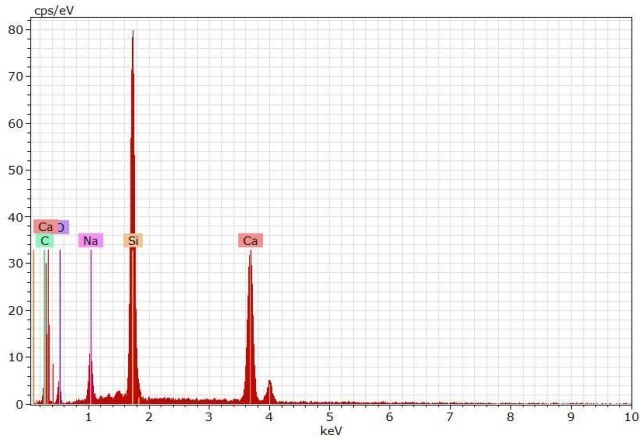

Figure 27: EDS spectra of the pectolite vein in sample MH-Q-1697.9; Note the presence of Na and the absence of Al.

Table 3: EMPA of prehnite on sample 1697.9 (wt% oxide); Nominal water content of 4.5 wt% taken from Deer, Howie and Zussman (2013). Formula based on 12 oxygens. Elemental values are calculated atomic formula units (i.e. cations per formula unit).

Scan #	1697.9.15	1697.9.9	1697.9.8	1697.9.10	1697.9.6	1697.9.5
SiO_2	43.94	43.13	42.39	42.03	47.41	46.74
Al_2O_3	22.82	23.66	22.89	22.80	20.19	19.10
CaO	25.83	25.91	25.94	26.25	27.58	27.80
Na_2O	0.00	0.00	0.00	0.00	0.09	0.11
K_2O	0.05	0.01	0.00	0.01	0.27	0.33
TiO_2	0.00	0.02	0.13	0.00	0.00	0.01
MgO	0.00	0.00	0.42	0.21	0.00	0.00
FeO	1.40	0.58	1.12	0.95	0.93	0.62
MnO	0.04	0.00	0.04	0.00	0.05	0.06
[H_2O*]	4.19	4.21	4.25	4.28	4.09	4.17
Total	103.08	102.32	101.92	101.25	105.51	103.75
Si	3.06	3.02	3.00	2.99	3.23	3.24
Al	1.87	1.95	1.91	1.91	1.62	1.56
Ca	1.93	1.94	1.96	2.00	2.01	2.07
Na	0.00	0.00	0.00	0.00	0.01	0.01
K	0.00	0.00	0.00	0.00	0.02	0.03
Mg	0.00	0.00	0.04	0.02	0.00	0.00
Fe	0.08	0.03	0.07	0.06	0.05	0.04
Mn	0.00	0.00	0.00	0.00	0.00	0.00
H	2.09	2.10	2.12	2.14	2.05	2.09
Sum	6.96	6.95	6.99	6.98	6.95	6.96

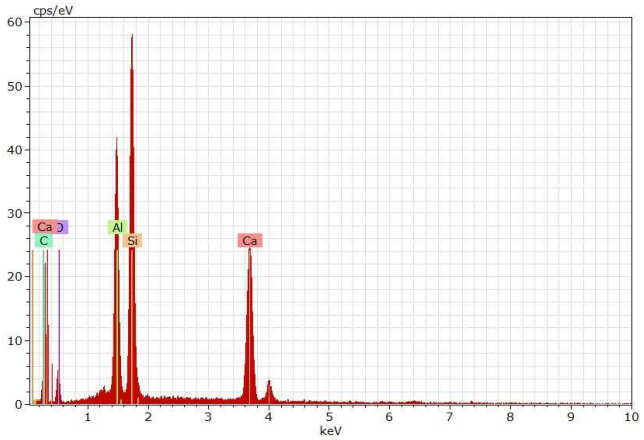

Figure 28: EDS spectra of the prehnite vein in sample MH-Q-1697.9; Note the presence of Al and the absence of Na.

Trace element content of calcite was determined by EMPA. Sample 1736 indicates minor amounts of Mn, Fe and Mg (Table 4) with increasing concentrations approaching the interface between calcite and altered basalt at the vein wall (Figure 24f).

Table 4: EMPA of calcite on sample 1736 (wt% oxide); Nominal CO_2 content of 44 wt% from ideal formula for calcite. Formula based on 6 oxygens. Elemental values are calculated atomic formula units (i.e. cations per formula unit).

Scan #	1736	1736.1	1736.2	1736.3
MgO	0.03	0.15	0.19	0.06
CaO	51.69	50.98	49.46	50.61
MnO	1.10	0.86	1.62	1.32
FeO	0.34	0.47	1.04	0.18
SrO	0.00	0.00	0.00	0.00
[CO_2*]	44.00	44.00	44.00	44.00
Total	97.16	96.46	96.31	96.17
Mg	0.005	0.024	0.030	0.010
Ca	5.867	5.856	5.728	5.854
Mn	0.099	0.078	0.148	0.120
Fe	0.030	0.042	0.094	0.016
Sr	0.000	0.000	0.000	0.000
Sum	6.001	6.000	6.000	6.000

4.5 CARBON AND OXYGEN STABLE ISOTOPE RATIOS

Analysis of the calcite $\delta^{18}O_{PDB}$ and $\delta^{13}C_{PDB}$ values for the 137 samples in the ZOI vary from -20.5 to -15.9 ‰ and -7.2 to -2.0 ‰, respectively (Figure 29, Table 5). There is overall greater variability in the data <1750 mbgs (standard deviations of 1.3 ‰ in $\delta^{13}C$ and 2.2 ‰ in $\delta^{18}O$) than there is deeper (standard deviations of 0.4 ‰ in $\delta^{13}C$ and 0.6 ‰ in $\delta^{18}O$) with notable increases in variability around 1709, 1720, and 1745 mbgs (Table 4).

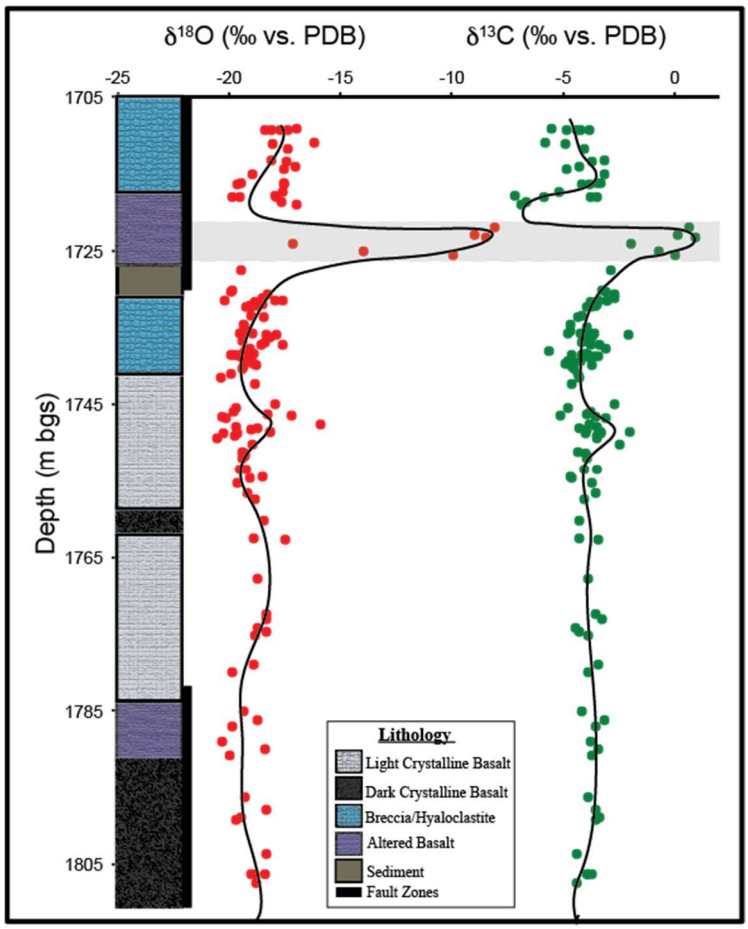

Figure 29: $\delta^{18}O_{PDB}$ and $\delta^{13}C_{PDB}$ vs. depth of the 137 MH-2 carbonate samples from 1709-1808 mbgs; The gray box outlines the zone of co-variation as described in section 5.3. The black line represents a running average of the data over this interval. Note the increased variability above 1750 mbgs.

Table 5: Ranges, means, and standard deviations of measured $\delta^{18}O$ and $\delta^{13}C$ values of the overall dataset and variation zones <1750 mbgs

Variation Zone (mbgs)	$\delta^{18}O_{PDB}$ Range	$\delta^{18}O$ Mean	SD	$\delta^{13}C_{PDB}$ Range	$\delta^{13}C$ Mean	SD
Overall	-20.5 to -15.9	-18.5	1.93	-7.2 to -2.0	-3.8	1.12
1709-1719	-19.9 to -16.2	-17.9	0.94	-7.2 to -3.2	-4.6	1.18
1720-1725	-17.1 to -8.10	-11.1	3.63	-1.9 to +0.88	-0.20	1.0
1740-1750	-20.5 to -15.9	-19.1	1.13	-5.1 to -2.0	-3.80	0.76

4.6 FLUID INCLUSION MICROTHERMOMETRY

Fluid inclusion homogenization and melting temperatures (T_h and T_m, respectively) were measured on MH-2 calcite samples to characterize the hydrothermal

fluid conditions during mineralization. Both primary and secondary fluid inclusions were measured. Distinguishing between primary and secondary inclusions was done following techniques described in Goldstein and Reynolds (1994) and Roedder (1984). Primary fluid inclusions are identified by their relationship to growth zonations, their random, isolated distribution, and relatively large sizes (Figure 30). They take almost any shape from globular to irregular. Growth zones bound primary inclusions indicating the origin is that of the primary fluid that was present during crystal growth and not those of secondary fluids. Alternatively, secondary fluid inclusions can cut across any or all growth zonations in a crystal (Figure 30). These usually occur in planar arrays along cleavage directions or twin planes. Their shape is usually round to sub-round but some often occur as flat elongate inclusions. These inclusions formed after crystal growth is complete and caused by fluid entrapment along healed micro-fractures or shear planes providing a record of the fluids present post crystal growth.

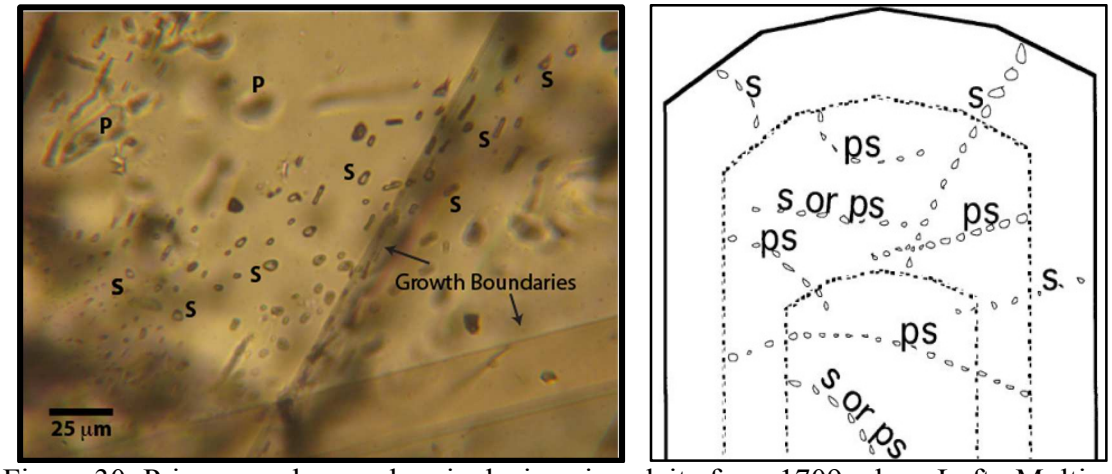

Figure 30: Primary and secondary inclusions in calcite from 1709 mbgs; Left: Multi-phase primary (P) and secondary (S) inclusions in calcite from the MH-2 core at 1709 mbgs (Plain-light, 50x); Right: Diagram from Goldstein and Reynolds (1994) illustrating the relationship between secondary and pseudosecondary fluid inclusions and crystal growth zones; Secondary inclusions cross growth zone boundaries while pseudosecondary inclusions do not.

Primary fluid inclusions in this study are irregularly shaped (Figures 31a-c) with some having a pyramidal to sub-pyramidal morphology (Figures 31d-e). Vapor-rich inclusions are also abundant throughout the ZOI (Figure 31a).

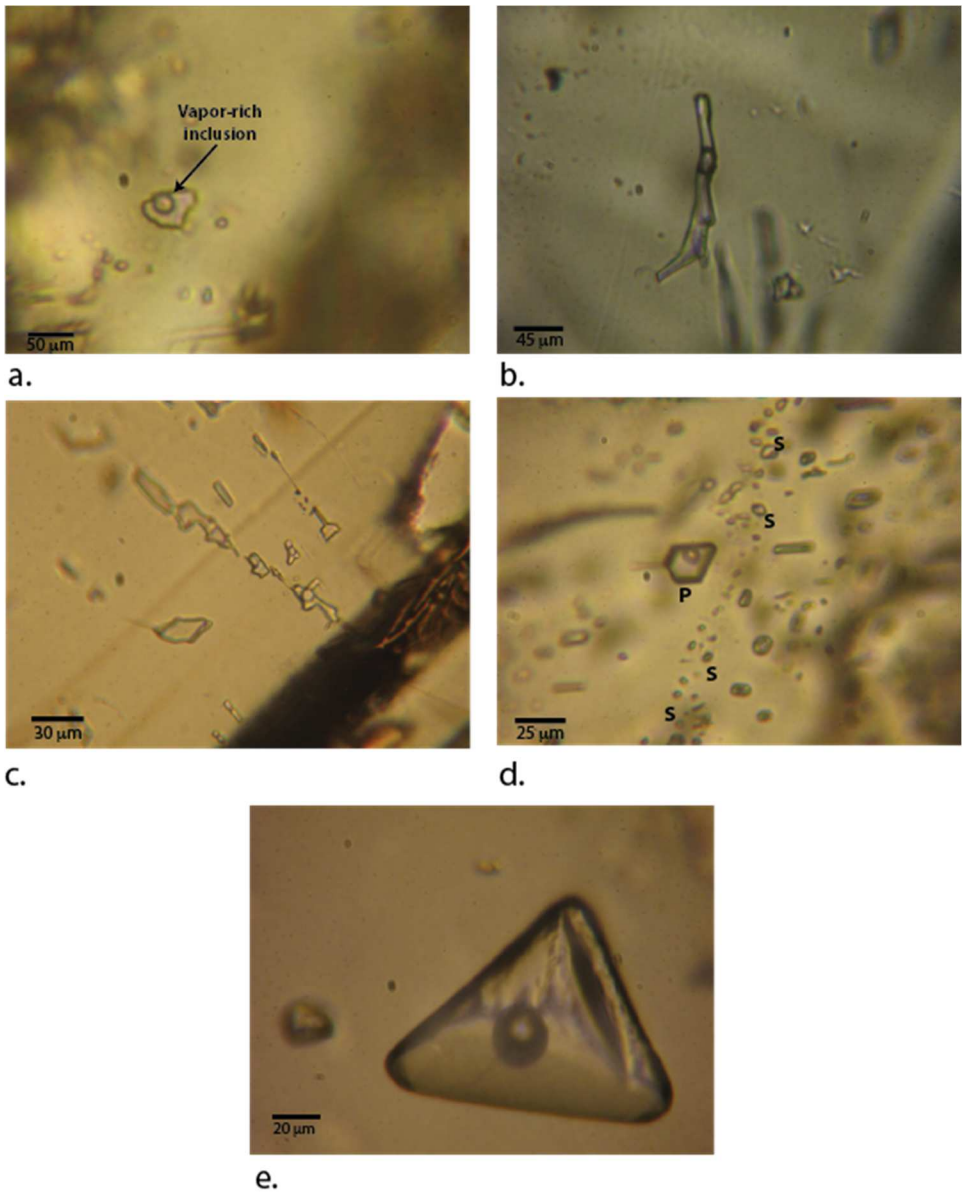

Figure 31: Plain light images of primary fluid inclusions in calcite from the MH-2 core; a: Vapor-rich fluid inclusion; b: Two-phase inclusion from at 1733 mbgs; c: Inclusions from 1789 mbgs; d: Inclusions from 1709 mbgs; Note the nature of the secondary inclusion trail to the right of the primary. e: Pyramidal inclusion. All inclusions are at 500x magnification

Secondary single and two-phase fluid inclusions are abundant and recognized as trails of fluid inclusions that cross growth zone boundaries (Figure 30). They are round to sub-rounded and often <10 μm in size making them difficult to make any observable measurements. Other secondary inclusions were flat and angular (Figure 32) to sub-angular and the majority range in size from 20-60 μm with some as large as 125 μm in the longest dimension.

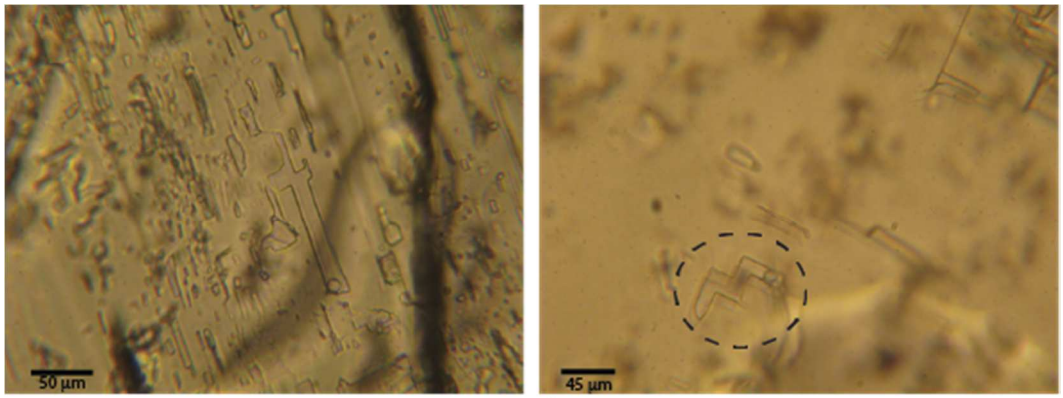

Figure 32: Plain light images of secondary fluid inclusions in calcite; a: 1734 mbgs; b: 1733 mbgs; Note the planar array of flat elongate inclusions with straight, sharp edges that indicate their secondary origin.

The primary inclusion T_h measurements from 34 inclusions (Figure 33) range from 126-358°C with three main populations: 147-200°C, 200-280°C, and 280-358°C and an average of 239°C. A subset of 11 primary inclusions, on which were performed more detailed analysis, were chosen to be representative of the whole (Table 5). Fewer inclusion measurements fall in the low and high temperature ranges with the majority of primary inclusions clustering in the intermediate temperature range of 200-280°C. T_h measurements of 24 secondary fluid inclusions revealed a range of 99-257°C with an

average of 153°C (Figure 34, Table 5). The majority of measurements range from 100-180°C and few measurements were made above 180°C.

There is an overlapping range of temperatures measured between primary and secondary inclusions and could possibly represent either: 1) that some calcite and primary inclusions were formed from which this same fluid produced secondary inclusions elsewhere, or 2) incorrect classification of some inclusions. Some of these inclusions may also be pseudosecondary inclusions and represent concurrent mineral growth and fluid entrapment along deformational fractures (Goldstein and Reynolds, 1994). Care was taken to minimize misidentification and errors in interpretation stemming therefrom should be small.

Table 6: Summary of fluid inclusion microthermometry in calcite mineralization of the MH-2 core

Sample I.D.	Depth (m)	Primary T_h (°C)	Secondary T_h (°C)	T_m (°C)	Salinity (wt% NaCl)
MH-C-FI-1709.2	1709	281	137	-0.7	1.25
MH-C-1711.1	1711.1	298	204	-0.8	1.40
MH-C-FI-1718.1	1718.1	287	146	-1.2	2.07
MH-C-1733.7	1733.7	251	127	-0.6	1.05
MH-C-FI-1734.6	1734.6	158	145	-0.3	0.53
MH-C-FI-1737.2	1737.2	228	126	-0.4	0.70
MH-C-FI-1738.6	1738.6	319	188	-0.5	0.88
MH-C-FI-1756	1756	203	147	-2.5	4.18
MH-C-FI-1789	1789	358	150	-0.3	0.53
MH-C-FI-1799	1799	147	138	-0.1	0.18
MH-C-FI-1806.4	1806	315	147	-0.3	0.53

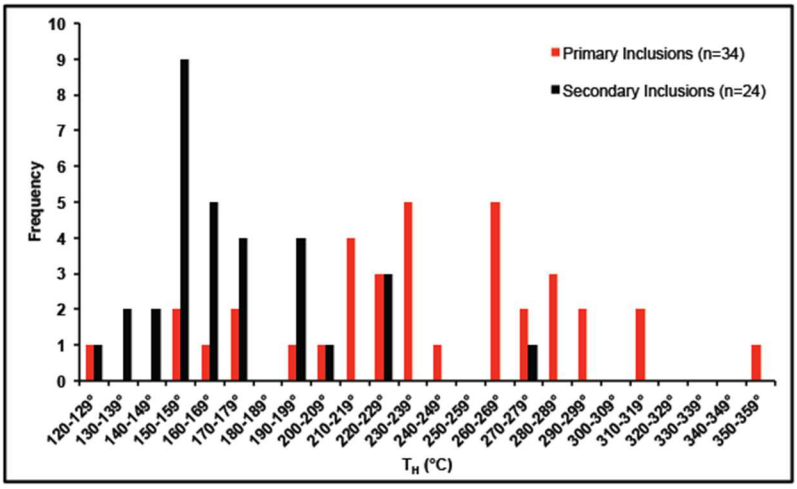

Figure 33: Distribution of primary (red) and secondary (black) inclusion T_h measurements in calcite samples from the MH-2 core

Complete freezing of 11 primary inclusions occurred between -38 and -40°C. The first melting temperatures could not be identified due to the lack of hydrohalite and apparent low salinities. The final melting temperatures (T_m) were recorded in a narrow range from -2.5 to -0.1°C. (1993) Bulk salinities were calculated assuming a H_2O-NaCl model composition and equation (8) from Bodnar (1993).

$$Salinity\ (wt\%\ NaCl) = 0.00 + 1.78\theta\ -\ 0.0442\theta^2 + 0.000557\theta^3 \qquad (8)$$

Based on the measured T_m (θ) of each sample, the salinity ranged from 0.18-4.18 wt % NaCl (Table 6, Figure 34).

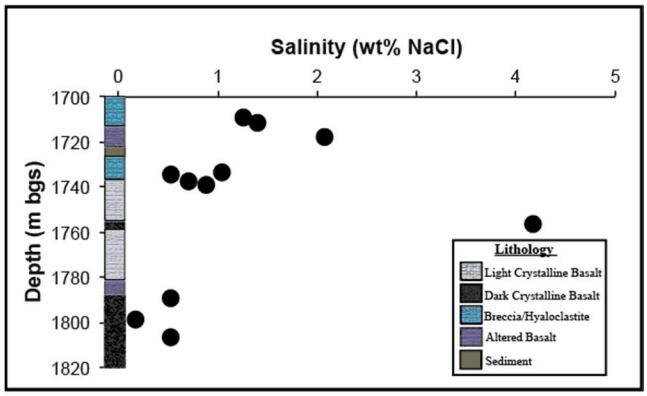

Figure 34: Salinity in the MH-2 primary fluid inclusions of calcite as a function of depth

5. DISCUSSION

Mineralization related to hydrothermal activity records thermal and compositional variations in past fluids of the MH geothermal system. Hydrothermal temperature estimates based on fluid inclusion trapping temperatures and mineral temperature stability ranges reveal that temperatures reached as high as ~370°C. Integration of these temperatures with a boiling point curve and core textural observations such as the presence of hydrothermal breccias suggests that boiling most likely occurred during peak hydrothermal temperatures. Stable isotope ratios of carbon and oxygen along with fluid inclusion measurements in calcite reveal that past fluids contained dissolved CO_2 with a magmatically derived component and contained low-moderate salinity. Calculated fluid $\delta^{18}O$ in combination with thermometry reveal a temporal cooling trend suggesting a waning heat source and mixing between meteoric groundwater and fluids that experienced high-temperature water-rock interaction due to crustal emplacement of magmatic material.

5.1 HYDROTHERMAL FLUID TEMPERATURES

MH calcite recording fluid temperatures have been precipitated over a range of temperatures (Figures 35 and 36). Temperature estimates were calculated using the method discussed in section 3.3.4 and result in T_t's of 183-425°C assuming a lithostatic pressure and 168-368°C assuming a hydrostatic pressure (Table 7). Although it is likely that the geothermal system is experienced pressures higher than hydrostatic (i.e. flowing waters from 1745 mbgs), a more conservative approach was chosen assuming that

hydrostatic pressure is dominating the system. Lithostatic and hydrostatic T_t's, therefore, represent end members for the fluids in question. There is no apparent correlation between T_t and depth (Figure 35).

Table 7: Calculated temperatures of trapping (T_t) from fluid inclusions in the MH-2 core

Sample I.D.	Primary T_t Lithostatic (°C)	Primary T_t Hydrostatic (°C)
MH-C-FI-1709.2	316	292
MH-C-1711.1	336	309
MH-C-FI-1718.1	323	298
MH-C-1733.7	283	262
MH-C-FI-1734.6	183	168
MH-C-FI-1737.2	258	239
MH-C-FI-1738.6	363	330
MH-C-FI-1756	231	213
MH-C-FI-1789	425	368
MH-C-FI-1799	194	177
MH-C-FI-1806.4	360	327

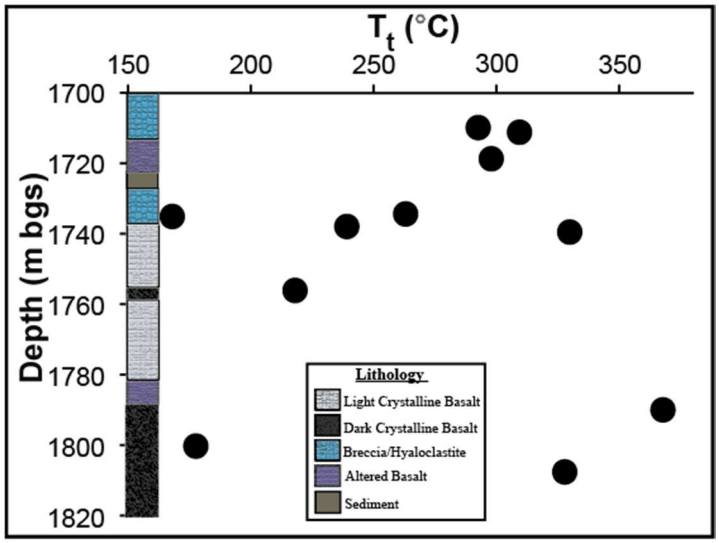

Figure 35: T_t as a function of depth derived from fluid inclusion measurements in calcite from the MH-2 core

Maximum temperatures observed (~370°C) are interpreted to have occurred early in the paragenesis. We interpret basalt breccias to represent early hydrothermal expansion at depth resultant from intense temperatures. This is evident from high

temperature fluid inclusions in calcite scattered throughout the ZOI along with basalt breccia observed in core. During this brecciation event, dissolved CO_2 levels in the circulating fluids were relatively high and calcite precipitation was abundant. Fluid inclusions in calcite indicate that it precipitated at temperatures ranging from 368-168°C. This is consistent with observed calcite temperature ranges within other geothermal systems (Browne, 1978, Simmons and Christenson, 1994). Pyrite also precipitated during this initial phase, possibly due to inputs of reduced sulfur from a magmatic source (e.g. H_2S) to oxygen poor waters (Bonatti et al, 1976).

In certain areas of the core, microcrystalline quartz is observed cross-cutting calcite (Figure 24b and d) indicating that after calcite precipitation, a silica-rich, and possibly cooler, fluid entered the system. Fluid inclusion measurements were difficult to make on this material and are not available to constrain the temperature of quartz precipitation. The temperatures of quartz precipitation are therefore constrained by temperatures of the fluid inclusions in the calcite it cross-cuts (maximum ~330°C).

Pectolite-prehnite is a mineral assemblage observed in a number of geothermal systems (Moller 1969, Leach and Rodgers, 1978, Neuhoff et al., 2006). Thermodynamic and experimental data constrain the temperature stability of pectolite to 200-400°C (Thilo and Funk, 1950, Yagi et al., 1968) Prehnite is stable at temperatures ranging between 300-350°C (Fyfe and Turner, 1958). Based on these observations and experiments, the fluids that precipitated the pectolite-prehnite in the MH core most likely were in the range of ~300-350°C (Figure 37). Cross-cutting relationships suggest that prehnite preceded pectolite. This suggests that after the aqueous Al^{3+} species (derived from alteration of

albite and/or clinopyroxene) were consumed as prehnite ($Ca_2Al(AlSi_3O_{10})(OH)_2$), precipitation of pectolite ($NaCa_2Si_3O_8(OH)$) occurred in the center of the veins (Figure 26e).

The pectolite-prehnite mineralization is physically separated from the majority of the calcite mineralization. Therefore, interpretation of the relative timing of the two assemblages is difficult. However, the measured temperatures in calcite and the assumed temperature stability of the pectolite-prehnite can be used to make a reasonable estimate. The pectolite-prehnite assemblage suggests three possible explanations: 1) the geothermal system in this zone was compartmentalized in the past with compositionally distinct waters; 2) the mineralization is recording a boiling process at depth that has striped the waters of the CO_2 necessary for calcite precipitation; or 3) CO_2 rich fluids at depth mixed with CO_2 poor fluids in this zone diluting the CO_2 concentration enough to prevent calcite mineralization. These possibilities cannot be further evaluated with the existing data.

The laumontite in the deeper parts of the core represents the final stage of mineralization and the lowest thermal regime recorded in mineralization due to cooling of the geothermal system. Its temperature stability has been documented in active geothermal systems and ranges from 75-224°C (Coombs et al., 1959, Seki et al., 1969) with most laumontite occurring below 200°C. It is rarely found in high temperature geothermal systems because above ~200°C it transitions to the less hydrated wairakite which is not documented in the MH-2 core.

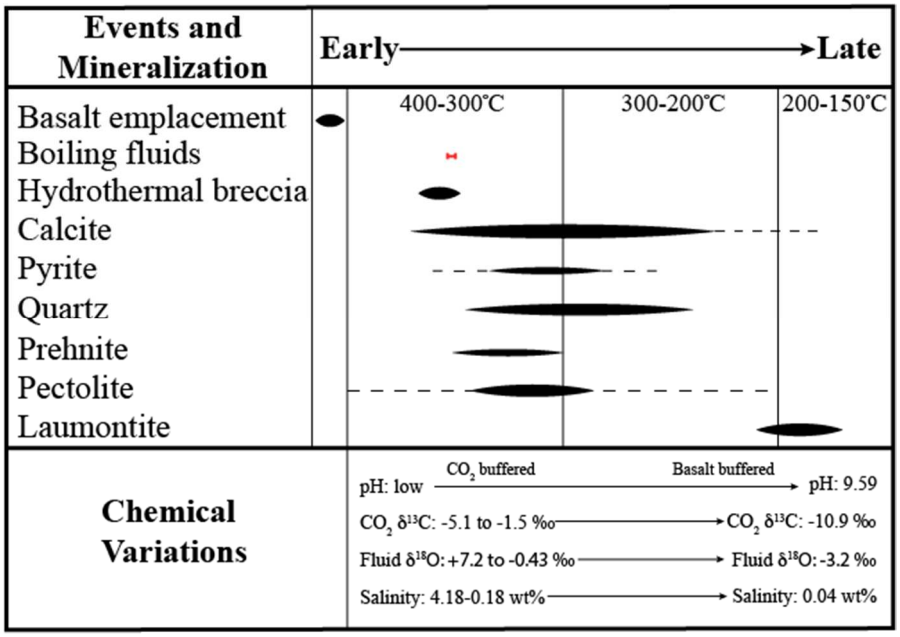

Figure 36: Paragenetic diagram illustrating key events in the history of mineralization in the MH-2 core

5.2 EVIDENCE OF BOILING

Evidence of boiling is recorded by multiple data sets and observations from the core: fluid temperatures, vapor rich inclusions, core textures, and stable isotopic variations. This evidence, plotted on the boiling point curve (BPC), illustrates early thermal conditions as the geothermal system began (Figure 37). The presence of hydrothermal breccias throughout the ZOI suggests that boiling may have occurred as high hydraulic pressures caused by thermal expansion of geothermal fluids (Nairn and Wiradiradja, 1980, Muffler et al., 1971, Hedenquist and Henley, 1985). Textural evidence indicates that shortly after brecciation, calcite precipitated and cemented the fragments in the voids. Based on the BPC assuming hydrostatic conditions (Figure 37), boiling in this zone of the borehole would require temperatures ~350-360°C, which is

consistent with the fluid inclusion microthermometry in calcite. Vapor-rich inclusions (Figure 31a) throughout the ZOI also support the concept of boiling within the system.

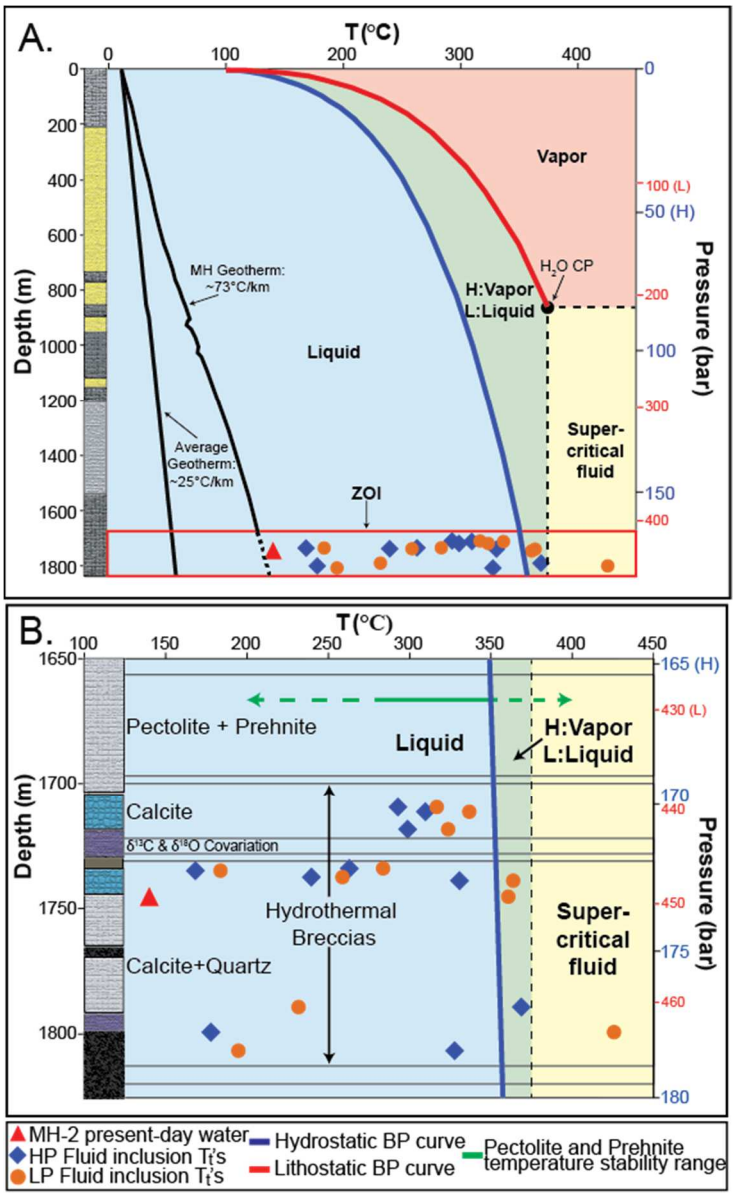

Figure 37: Boiling point curves and water phase diagrams and with relation to MH and zones of mineralization and fluid inclusion measurements; A-Hydrostatic and lithostatic boiling point curves (BPC) and water phase diagram for the entire MH-2 core; H represents hydrostatic conditions and L represents lithostatic conditions. B-ZOI plotted with the BPC curve, zones of secondary mineralization, rock textures, hydrostatic (HP) and lithostatic (LP) fluid inclusion T_t's, MH present-day water, and zone of isotopic co-variation in the MH-2 core; Note the proximity of the high temperature fluid inclusions to the BPC.

In this study, the peak temperature of the MH geothermal system was approximately 368°C. This is the only measurement that exceeds the BPC and the majority of the fluid inclusions indicate temperatures lower than boiling. There is some uncertainty due to the assumption of hydrostatic pressure for both the BPC and pressure correction of fluid inclusion T_h. Pressures higher than hydrostatic could result in fluid inclusion temperatures plotting closer to the BPC. This in turn would steepen the BPC to somewhere in between the hydrostatic and lithostatic curves (Figure 37a, blue and red curves, respectively). This suggests that the actual fluid inclusion temperatures of trapping are likely bounded by the hydrostatic and lithostatic temperatures (Figure 37, blue and orange points, respectively)

During boiling, steam separation, and degassing, lighter isotopes preferentially partition (^{16}O and H in water, ^{12}C in CO_2) into the vapor/gas phase (Giggenbach, 1992, Boles, 2004, Dobson, 2003). Due to the likely rapid and unidirectional nature of this reaction, non-equilibrium fractionation will occur. This non-equilibrium fractionation could describe the zone in which $\delta^{18}O$ and $\delta^{13}C$ co-vary (Figures 29 and 38). Throughout this narrow zone, the rock is a fine grained, friable, highly altered basaltic sandstone, breccia, and hyaloclastite that lack developed fractures. Unconfined uniaxial compressive stress experiments identified this as part of a zone with the lowest density rock type, the weakest under stress, and one of the most permeable zones throughout the bottom part of the MH-2 core (Kessler, 2014). This increase in permeability could have allowed for rising geothermal waters to depressurize quickly resulting in boiling, fluid degassing and associated non-equilibrium fractionation. Rapid calcite precipitation due

to this change in rock type, decrease of pressure, and CO_2 loss could explain such isotopic co-variation.

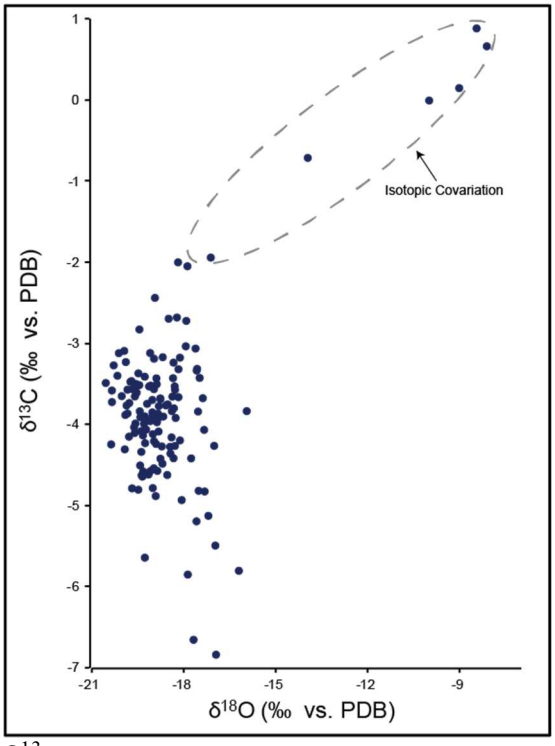

Figure 38: $\delta^{18}O_{PDB}$ and $\delta^{13}C_{PDB}$ of calcite from the MH-2 core; Note the variation (gray ellipse).

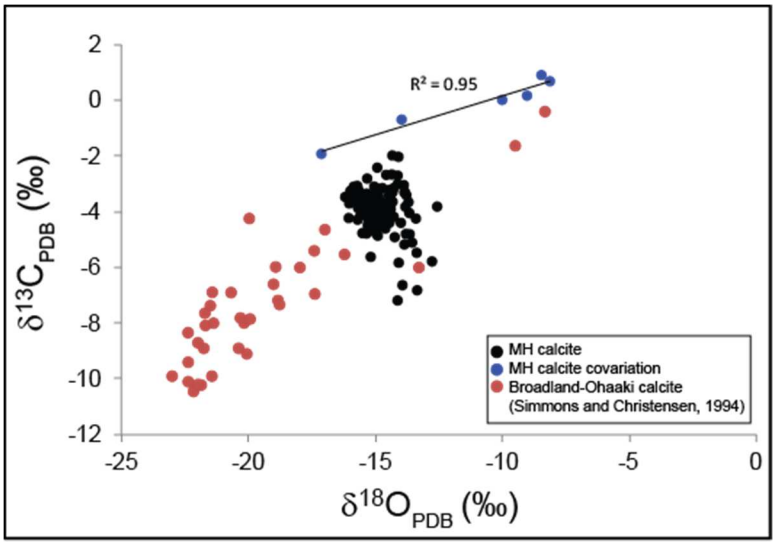

Figure 39: $\delta^{18}O_{PDB}$ and $\delta^{13}C_{PDB}$ values in calcite from the MH-2 core and Broadlands-Ohaaki geothermal system in New Zealand representing varying degrees of isotopic fractionation due to boiling; Note the strong correlation in the co-variation samples (blue) from the MH calcite.

There is a strong correlation between $\delta^{18}O$ and $\delta^{13}C$ (R^2=0.95) (Figure 39) suggesting that isotopic fractionation occurred in both systems. In geothermal systems of New Zealand, enrichments in geothermal fluid ^{18}O have been attributed to boiling (Figure 60, Simmons and Christenson, 1994). When compared to the values from New Zealand, the $\delta^{18}O$ and $\delta^{13}C$ in all MH calcite samples appear to follow a similar trend.

5.3 PALEO-FLUID COMPOSITION AND ORIGIN

5.3.1 Dissolved Carbon

Stable isotopes of carbon in hydrothermally precipitated calcite can be used to constrain paleo-water dissolved carbon origins and possible CO_2 source inputs. With the exception of the co-variation zone, the $\delta^{13}C_{PDB}$ in MH calcite ranges from -7.2 to -2.0 ‰. Temperature dependence in carbon fractionation between CO_2 and calcite (Equation 9) leads to calculated $\delta^{13}C_{CO2}$ values that range from -5.1 to -1.5 ‰.

$$1000ln\alpha \sim \Delta = \delta^{13}C_{CO2} - \delta^{13}C_{cc} = -2.4612 + \frac{7.6663*10^3}{T} - \frac{2.988*10^6}{T^2}$$

(Bottinga, 1968) (9)

Upper mantle $\delta^{13}C_{CO2}$ values range from -8.5 to -3.5 ‰ (Javoy et al., 1986) with a tighter range of -6.0 to -5.0 ‰ being reported by Sharp (2007). Axial rift zone geothermal fluids in Iceland reveal mantle CO_2 signatures from -5.1 to +2.9 ‰ (Barry et al., 2014). Calculated $\delta^{13}C_{CO2}$ values of this study are in the range of upper mantle CO_2 with the higher values possibly representing progressive mineralization from a fluid, mixing, and boiling/degassing (Javoy et al., 1978, Barry et a., 2014, Macpherson et al., 2010, Furi et al., 2010). Mixing of CO_2 from assimilation, decarbonation, or

hydrothermal alteration and dissolution of deep carbonates as magma rose into the crust could produce similar signatures. Although marine limestones and calc-silicate marbles are inferred in some cross sections (e.g. Lewis et. al, 2012) in the deep basement, these interpretations are not based on subsurface data. With the lack of data and nearby surface exposures, it is unlikely that carbonates are present beneath this part of the WSRP. I suggest that the MH calcite represents precipitation from fluids containing mantle derived (i.e. magmatic) CO_2.

Over time, the flux of deeply derived carbon into the system appears to have decreased. Today's water is -10.9 ‰ in $\delta^{13}C$ whereas MH calcites reflect $\delta^{13}C_{CO2}$ values of -5.1 to -1.5 ‰. This implies that magmatic CO_2 recorded in calcite has changed since the time of mineralization. Due to this decrease in CO_2, calcite precipitation has most likely ceased as well. The present water is low in dissolved carbonate (100 ppm, Lachmar et al., 2012) and geochemical modeling using PHREEQC indicates that the water is under-saturated with respect to calcite suggesting little potential for calcite mineralization. Based on this change, the MH geothermal system seems to have experienced temporal cooling, CO_2 loss, and dilution with other waters.

5.3.2 Groundwater Source and Evolution

The $\delta^{18}O_{PDB}$ in MH calcite veins varies between -20 and -16 ‰. Hydrothermal fluid temperatures (T_t) determined by microthermometry were used to calculate the $\delta^{18}O_{SMOW}$ of the fluid using a temperature dependent equilibrium fractionation equation between calcite and water (Equation 10). Using equations 10 and 11 with microthermometry fluid temperatures (168-368°C) the resulting water $\delta^{18}O_{SMOW}$ ranges

from -0.43 to +7.2 ‰. For comparison, modern meteoric water $\delta^{18}O_{SMOW}$ in the SRP ranges from -19 and -16 ‰ (Wood and Low, 1986).

$$1000ln\alpha = \frac{2.78\times10^6}{T^2} + 2.89 \quad \text{(O'Neil, 1969 and 1975)} \qquad (10)$$

$$1000ln\alpha = \Delta_{cc-H_2O} = \delta^{18}O_{cc} - \delta^{18}O_{H_2O} \qquad (11)$$

A correlation (r^2=0.78) is observed between paleo-water oxygen isotope composition and temperature of calcite mineralization (Figure 40). Including the present-day MH-2 water temperature and composition slightly improves this correlation (0.83). This data excludes the co-variation zone due to the likelihood of non-equilibrium fractionation. No apparent correlation is recognized between fluid inclusion paleo-isotopic composition and depth (Figure 41).

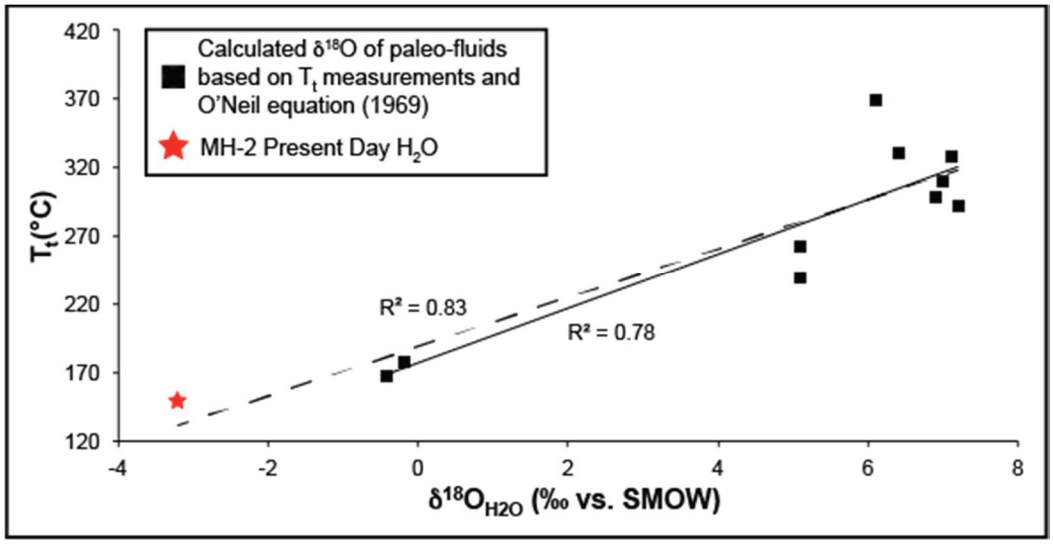

Figure 40: Calculated of paleo-fluids as a function of T_t calculated in primary inclusions of calcite in the MH-2 core along with MH-2 present-day water composition and temperature; Linear regressions suggest temporal cooling of the geothermal system.

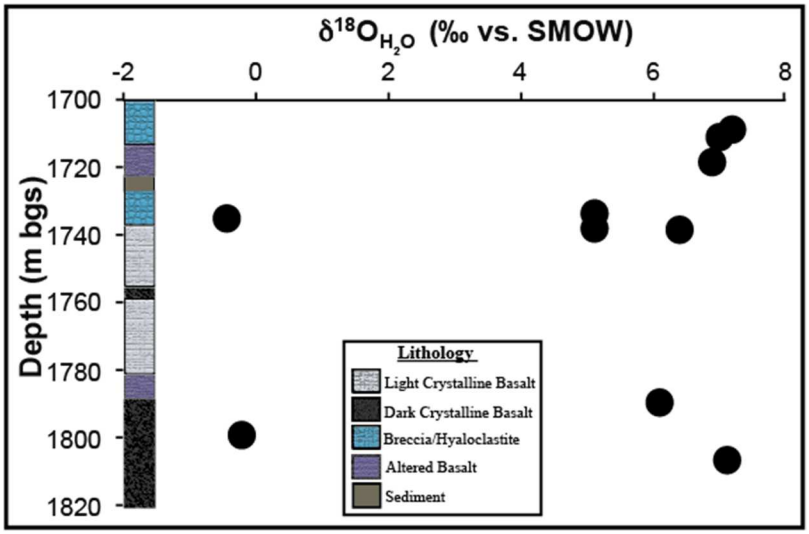

Figure 41: $\delta^{18}O_{SMOW}$ of paleo-fluids between 1700 and 1820 mbgs in MH-2; These compositions are calculated using calcite $\delta^{18}O$ and associated fluid inclusion T_t.

Two main isotopic compositions are observed from figure 41. The higher temperatures cluster at the positive end of $\delta^{18}O$ values and the lower temperatures correlate with the negative $\delta^{18}O$ values. The present-day MH-2 water falls on an apparent mixing trend between -20 and +7.2 ‰ in $\delta^{18}O$ and -150 to -60 ‰ in δD suggesting extensive water-rock interaction and enrichment of ^{18}O and ^{2}H (Figure 42). Paleo-fluid compositions (gray box) of calculated $\delta^{18}O$ from fluid inclusions and δD bounded by regional and magmatic fluid δD plot between the present-day water and magmatic fluid box. This suggests a mixture between meteoric groundwater and fluids associated with high temperature water-rock interaction related to an intrusive body (Giggenbach, 1992). For comparison, thermal and mineral waters from the Yellowstone region can be explained by high temperature exchange between meteoric water and hot silicate bedrock (Kharaka, 2002). MH geothermal fluids exhibited high $\delta^{18}O$ while the system was at its peak temperature of approximately 368°C and over time, as the

geothermal system cooled down, less magmatic input and water-rock interaction caused the fluids to progressively evolve toward the present-day composition (-3.2 ‰ SMOW).

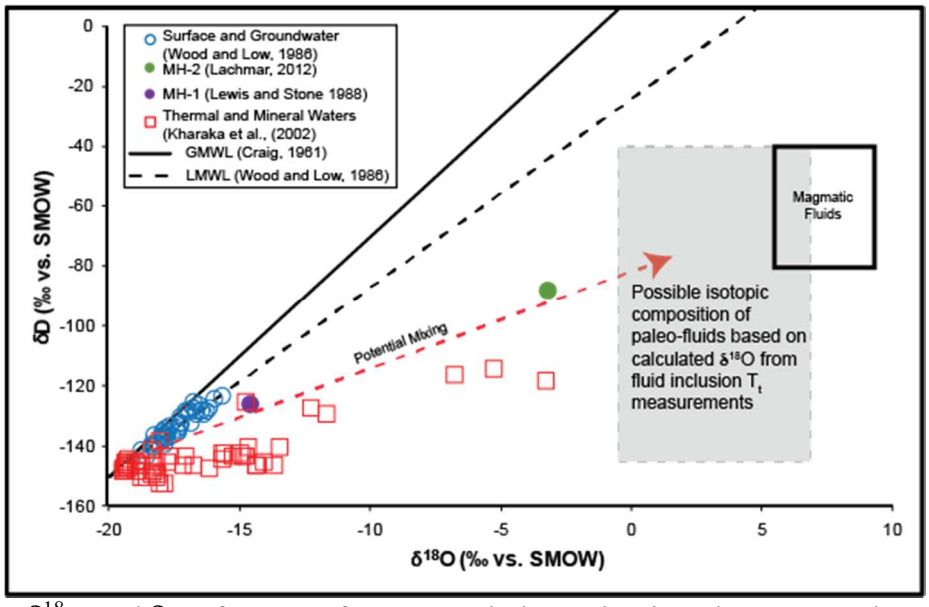

Figure 42: $\delta^{18}O$ and δD of SRP surface, ground, thermal, mineral, MH-1, and MH-2 waters; Global Meteoric Water Line ($\delta D=8.0*\delta^{18}O+10$ ‰ from Craig, 1961) and the Local Meteoric Water Line ($\delta D=6.3*\delta^{18}O-24$ ‰ from Wood and Low, 1986) are plotted for comparison. Also plotted are the calculated $\delta^{18}O$ and possible δD compositions of paleo-fluids (gray box) representing the range of calculated paleo-fluid $\delta^{18}O$ values from this study and possible associated δD values constrained by local meteoric compositions and potential magmatic fluid δD. Note the trend toward the magmatic water box (Giggenbach, 1992).

5.3.3 Groundwater Salinity

Geothermal fluid salinities related to magmatic systems can range from hypersaline (> 50 wt %) to low (<5 wt%) to very low (0.2-0.5 wt%) depending on melt type and subsurface conditions such as depth, pressure, temperature, and composition of host rock that has interacted with the fluids in the past. In contrast, most sedimentary basin brines are hypersaline due to long-lived, hot water-rock interaction and high primary fluid salinity (i.e. seawater). Also for comparison, the salinity of most shallow

groundwater is dilute (0.035 wt%, Langmuir, 1997) and MH groundwater ranges from 0.02-0.05 wt% (Young, 1977, Lachmar et al., 2012, Freeman, 2013). The salinity measurements for MH fluid inclusions (0.18-4.18 wt % NaCl) are similar to the relatively low values reported for some magmatic systems (Hedenquist and Lowenstern, 1994) but much higher than present-day. Thus, it is plausible that the MH water has a magmatic component to the salinity that was diluted by various proportions of meteoric groundwater.

5.4 SOURCE AND TIMING OF HYDROTHERMAL ACTIVITY

Strong evidence exists that the mineralization and alteration observed in the Mountain Home core was the result of hydrothermal fluid circulation at depth postdating eruptions of the basalts, and not the product of near-surface water-rock interaction related to the eruption of basalts. The high temperatures recorded by fluid inclusions, mineral paragenesis, and the presence of hydrothermal breccias (Fig. 37) require deep hydrothermal activity. These high fluid temperatures (up to ~370°C) far exceed shallow boiling temperatures (Figure 37), and would have resulted in rapid flashing to steam creating phreatomagmatic eruptions and textures in the recovered core such as in New Zealand (Browne and Lawless, 2001). Although hydrothermal breccias are common in near-surface hydrothermal steam eruptions, they describe these deposits as typically poorly sorted, matrix supported, fine-grained material with evidence of ejecta fragments within the matrix. Fluid inclusions would also likely be sparse due to such violent volcanism. If these alteration textures and veins were formed near the surface (~50 m)

related to heat generated by eruption of the basalts on the surface, fluid inclusion temperatures should record much more moderate temperatures (<150°C).

Given the tectonic setting and the composition of relic geothermal fluids, a magmatic event likely provided the necessary heat and fluids to the system. The host basalt of the MH geothermal system has been dated at approximately 9 Ma (Jenks and Bonnichsen, 1989, Wood and Clemens, 2002, White and Hart, 2002, Bonnichsen and Godchaux, 2002). Younger basalt volcanism started ~800 ka with the youngest vents in the WSRP dated at ~100 ka (Shervais and Vetter, 2009). It is likely that during one of these pulses of youngest volcanism, magma intruded into the crust in this part of the WSRP supplying the geothermal heat and fluids observed in mineralization of the MH-2 core. A layered mafic sill complex, similar to what is interpreted in the ESRP, could have developed during the youngest volcanism providing a self-insulated intrusion that provided a longer-lived heat source than those usually associated with basaltic magma systems. As this magmatic system waned, the temperatures cooled down and magmatic fluid inputs decreased eventually evolving toward the present-day temperature and composition.

6. SUMMARY

Multiple geological and geochemical techniques are used to describe a fossil basalt-hosted geothermal system in the subsurface beneath the WSRP. Hydrothermal brecciation occurred early in the history of the system when temperatures were highest. Calcite began precipitation at this time and dominates throughout most of the ZOI. It was then followed by prehnite and pectolite in the upper section based on textural observations and mineral temperature stability ranges. Quartz precipitation occurred in parts of the deeper section as is evident from textural relationships with calcite. Laumontite finally precipitated from late geothermal fluids and is observed on core surfaces.

Fluid inclusion microthermometry indicates that the temperature of the past hydrothermal waters ranged from 168-368°C, consistent with the temperature stability of observed secondary mineralization. Boiling in the geothermal system may have occurred at the peak temperature and is supported by the presence of hydrothermal breccias, vapor-rich fluid inclusions, and evidence for non-equilibrium fractionation in certain zones of calcite mineralization. This boiling is interpreted to have occurred at depth and not near the surface due to evidence in the rock textures and fluid inclusions. Carbon and oxygen isotope ratios suggest that calcite precipitated at depth from fluids that represent a mixture of deep-seated mantle derived and meteoric fluids along with high temperature water-rock interaction throughout the life of the geothermal system. Paleo-fluid oxygen isotope compositions calculated using a calcite-water geothermometer and fluid inclusion

measurements suggests that over time the geothermal system has been cooling down and mixing with meteoric groundwater.

Blind basalt-hosted geothermal systems that lack surficial manifestations can be difficult to assess. Many methods are being employed to understand them including traditional geothermometry and multicomponent mineral equilibrium geothermometry. This study indicates that basalt-hosted systems have the potential to be a hot water geothermal resource (Figure 9) similar to those in Iceland or Hawaii. By using techniques described in this study, an understanding of the past geothermal conditions and temporal/compositional evolution can be attained. When unknown basalt-hosted blind geothermal systems yield their abundance and become known through applications of strategies and geochemical approaches such as this, the geothermal future of the nation will become clearer and brighter.

7. REFERENCES

Arney, B.H., Gardner, J.N., and Belluomini, S.G., 1984, Petrographic analysis and correlation of volcanic rocks in Bostic 1-A well near Mountain Home, Idaho: Los Alamos National Laboratory Report LA-9966-HDR, 29 p.

Armstrong, J., Breckenridge, R.P., Dumont, S.A., Kessler, J., Lachmar et al., T., Mines, G., Nielson, D., Schmitt, D., Shervais, J.W., and Wood, T.R., 2013, Mountain Home Air Force Base, Idaho Geothermal Resource Assessment and Future Recommendations, Idaho National Laboratory Report INL/EXT-12-26319, 74 p.

Bakker, R.J., 2003, Package FLUIDS 1, Computer programs for analysis of fluid inclusion data and for modeling bulk fluid properties, Chemical Geology, v. 194, p. 3-23, http://fluids.unileoben.ac.at/Computer.html.

Barry, P.H., Hilton, D.R., Furi, E., Halldorsson, S.A., and Gronvold, K., 2014, Carbon isotope and abundance systematics of Icelandic geothermal gases, fluids and subglacial basalts with implications for mantle plume-related CO_2 fluxes, Geochimica et Cosmochimica Acta, v. 134, p. 74-99.

Beaufort, D., and Meunier, A., 1994, Saponite, corrensite, and chlorite-saponite mixed layers in the Sancerre-Couy deep drill-hole (France), Clay Minerals, v. 29, p. 47-61.

Bettison-Varga, L., and Mackinnon, I. D. R., 1997, The role of randomly mixed-layered chlorite/smectite in the transformation of smectite to chlorite, Clays and Clay Minerals, v. 45, p. 506-516.

Bodnar, R.J., 1993, Revised equation and table for determining the freezing point

depression of H_2O-NaCl solutions, Geochimica et Cosmochimica Acta, v. 57, p. 683-684.

Bodnar, R.J., and Vityk, M.O., 1994 Interpretation of microthermometric data for H_2O-NaCl fluid inclusions, *in* Fluid Inclusions in Minerals, Methods and Applications, De Vivo, B., and Frezzotti, M.L. eds., Virginia Tech, Blacksburg, VA, p. 117-130.

Bonatti, E., Honnorez-Guerstein, M.B., Honnorez, J., and Stern, C., 1976, Hydrothermal pyrite concretions from the Romanche trench (equatorial Atlantic): metallogenesis in oceanic fracture zones, Earth and Planetary Science Letters, v. 32, p. 1-10.

Bird, D.K., Schiffman, P., Elders, W.A., Williams, A.E., and McDowell, S.D., 1984, Calc-silicate mineralization in active geothermal systems, Economic Geology, v. 79, p. 671-695.

Blackwell, D.D., Richards, M.C., Frone, Z.S., Batir, J.F., Williams, M.A., Ruzo, A.A., and Dingwall, R.K., 2011, SMU Laboratory Heat Flow Map of the Conterminous United States, supported by Google.org. http://www.smu.edu/geothermal.

Blackwell, D.D., 1989, Regional implications of heat flow of the Snake River Plain, Northwestern United States, Tectonophysics, v. 157, p. 241-250.

Boles, J.R., 2004, Rapid growth of meter-scale calcite speleothems in the Mission Tunnel, Santa Barbara, CA, *in* Proceedings, Eleventh International Symposium on Water-Rock Interaction, Saratoga Springs, New York, USA, v. 1, p. 353-356.

Bonnichsen, B., Godchaux, M.M., 2002, Late Miocene, Pliocene, and Pleistocene geology of southwestern Idaho with emphasis on basalts in the Bruneau–Jarbidge,

Twin Falls, and western Snake River Plain regions. In Bonnichsen, B., White, C.M., McCurry, M., (eds), Tectonic and Magmatic Evolution of the Snake River Plain Volcanic Province: Idaho. Geological Survey Bulletin, v. 30, p. 233–312.

Browne, P.R.L., 1978, Hydrothermal alteration in active geothermal fields, Annual Reviews in Earth and Planetary Science, v. 6 p. 229-250.

Browne, P.R.L., and Ellis, A., 1970, The Ohaaki-Broadlands hydrothermal area, New Zealand: Mineralogy and related geochemistry. American Journal of Science, v. 269, p 97-131.

Browne, P.R.L., and Lawless, J.V., 2001, Characteristics of hydrothermal eruptions, with examples from New Zealand and elsewhere, Earth-Science Reviews, v. 52, p. 299-331.

Cartigny, P., Jendrzejewski, N., Pineau, F., Petit, E., and Javoy, M., 2001, Volatile (C, N, Ar) variability in MORB and the respective roles of mantle source heterogeneity and degassing: the case of the Southwest Indian Ridge, Earth and Planetary Science Letters, v. 194, p. 241-257.

Coombs, D.S., Ellis, A.J., Fyfe, W.S., and Taylor, A.M., 1959, The zeolite facies, with comments on the interpretation of hydrothermal syntheses, Geochimica et Cosmochimica Acta, v. 17, p. 53-107.

Craig, H., 1961, Isotopic variations in meteoric waters, Science, v. 133, p. 1702-1703.

Davies, J.H., Davies, D.R., 2010, Earth's surface heat flux, Solid Earth, v. 1, p. 5-24

Deer, W.A., Howie, R.A., and Zussman, J., 2013, Introduction to the rock forming minerals: Third Edition, Mineralogical Society, London, 510 p.

DeNosaquo, K.R., Smith, R.B., and Lowry, A.R., 2009, Density and lithospheric strength models of the Yellowstone-Snake River Plain volcanic system from gravity and heat flow data, Journal of Volcanology and Geothermal Research, v. 188, p. 108-127.

Dobson, P.F., Kneafsey, T.J., Hulen, J., and Simmons, A., 2003, Porosity, permeability, and fluid flow in the Yellowstone geothermal system, Wyoming, Journal of Volcanology and Geothermal Research, v. 123 p. 313-324.

Duchane, D., and Brown, D., 2000, Hot dry rock geothermal energy development in the USA, Los Alamos National Laboratory. 20 p.

Duffield, W.A., and Sass, J.H., 2003, Geothermal energy-clean powered from the Earth's heat, U.S. Geological Survey, Circular 1249, 43 p.

Ekren, E.B., McIntyre, D.H., Bennett, E.H., and Marvin, R.F., 1982, Cenozoic stratigraphy of western Owyhee County, Idaho, *in* Bonnichsen, W. and Breckenridge, R.M. eds. Cenozoic Geology of Idaho, Idaho Bureau of Mines and Geology Bulletin 26, p. 215-236.

Elders, W.A., Fridleifsson, G.U., and Albertsson, A., 2014, Drilling into magma and the implications of the Iceland Deep Drilling Project (IDDP) for high-temperature geothermal systems worldwide, Geothermics, v. 49, p. 111-118.

Ellis, A.J., and Mahon, W.A.J., 1977, Chemistry and geothermal systems: New York, Academic Press, 392 p.

Ferguson, G., Grasby, S.E., and Hindle, S.R., 2009, What do aqueous geothermometers really tell us?, Geofluids, v. 9, p. 39-48.

Fournier, R.O., 1973, Silica in thermal waters: Laboratory and field investigations, Biogeochemistry, p. 122-139.

Fournier R.O., 1981, Application of water geochemistry to geothermal exploration and reservoir engineering: *in* Geothermal Systems Principles and Case Histories, Ryback and Muffler, eds: John Wiley and Sons, NY, p. 109-143.

Fournier R.O., and Potter, R.W. II, 1982, A revised and expanded silica (quartz) geothermometer: Geothermal Resources Council Bulletin, v.1, p. 3-12.

Freeman, K.G., 2013, Evaluation of the geothermal potential of the Snake River Plain, Idaho, based on three exploration holes, [M.S. Thesis], Utah State University. 102 p.

Furi E., Hilton D. R., Halldorsson S. A., Barry P. H., Hahm D., Fischer T. P., and Gronvold K., 2010, Apparent decoupling of the He and Ne isotope systematics of the Icelandic mantle: the role of He depletion, melt mixing, degassing fractionation and air interaction. Geochimica et Cosmochimica Acta v. 74, p. 3307–3332.

Fyfe W.S., and Turner, F.J., 1958, Correlation of metamorphic facies with experimental data, *in* Fyfe W.S., Turner, F.J., and Verhoogen, J., 1958, Metamorphic reactions and metamorphic facies, Geological Society of America Memoir 73, p. 1-251.

Giggenbach, W.F., 1980, Geothermal gas equlibria: Geochimica et Cosmochimica Acta, v. 44, p. 2021-2023.

Giggenbach, W.F., 1988, Geothermal solute equilibria: Derivation of Na–K–Mg–Ca geoindicators, Geochimica et Cosmochimica Acta, v. 52, p. 2749-2765.

Giggenbach, W.F., 1991, Chemical techniques in geothermal exploration: *in* Application of Geochemistry in Resources Development, UNITAR/ UNDP Guidebook, p. 119-144.

Giggenbach, W.F., 1992, Isotopic shifts in waters from geothermal and volcanic systems along convergent plate boundaries and their origin, Earth and Planetary Science Letters, v. 113, p. 495-510.

Goldstein, R.H. and Reynolds, T.J., 1994, Systematics of fluid inclusions in diagenetic minerals, Society of Sedimentary Geology Short Course 31, 213 p.

Gupta, H.K., and Roy, S., 2007, Geothermal Energy: An Alternative Resource for the 21st Century, Elsevier, Amsterdam, 292 p.

Hedenquist, J.W., Henley, R.W., 1985, Hydrothermal eruptions in the Waiotapu geothermal system, New Zealand; their origin, associated breccias, and relation to precious metal mineralization, Economic Geology, v. 80, p. 1640-1668.

Hedenquist, J.W., Lowenstern, J.B., 1994, The role of magmas in the formation of hydrothermal ore deposits, Nature, v. 370, p. 519-527.

Hot Dry Rock Assessment Panel, 1977, Hot dry rock geothermal energy: status of exploration and assessment, Report no. 1 of the Hot Dry Rock Assessment Panel, 228 p.

Javoy M., Pineau F., and Iiyama I., 1978, Experimental determination of the isotopic fractionation between gaseous CO_2 and carbon dissolved in tholeiitic magma; a preliminary study. Contributions to Mineralogy and Petrology, v. 67, p. 35–39.

Javoy, M., Pineau, F., and Delorme, H., 1986, Carbon and Nitrogen Isotopes in the

Mantle, Chemical Geology, v. 57, p. 41-62.

Jenks, M.D., and Bonnichsen, B., 1989, Subaqueous basalt eruptions into Pliocene Lake Idaho, Snake River Plain, Idaho, *in* V.E. Chamberlain, R.M. Breckenridge, and Bill Bonnichsen, eds., Guidebook of the Geology of Northern and Western Idaho and Surrounding Areas, Idaho Geological Survey Bulletin 28, p. 17-34.

Keith, T.E.C., and Muffler, J.P., 1978, Minerals produced during cooling and hydrothermal alteration of ash flow tuff from Yellowstone drillhole Y-5, Journal of Volcanology and Geothermal Research, v. 3, p. 373-402.

Keith, T.E.C., White, D.E., and Beeson, M.H., 1978, Hydrothermal alteration and self-sealing in Y-7 and Y-8 drillholes in northern part of Upper Geyser Basin, Yellowstone National Park, Wyoming, USGS Professional Paper 1054A, 13 p.

Keller, E.A., 2000, Environmental Geology Edition 8, Prentice Hall. 624 p.

Kessler, J.A., 2014, In-situ stress and geology from the MH-2 Borehole, Mountain Home, Idaho: Implications for geothermal exploration from fractures, rock properties and geomechanics [PhD thesis] Utah State University.

Kharaka, Y.K., Thordsen, J.J., and White, L.D., 2002, Isotope and chemical compositions of meteoric and thermal waters and snow from the greater Yellowstone National Park Region, U.S. Geological Survey, Open File Report 2002-194, 75 p.

Knight, C.L., and Bodnar, R.J., 1989, Synthetic fluid inclusions IX, Critical PVTX properties of NaCl-H2O solutions, Geochimica et Cosmochimica Acta, v. 53, p. 3-8.

Lachmar, T.E., Freeman, T.G., Wood, T.R., Shervais, J.W., and Nielson, D.L., 2012,

Chemistry and thermometry of geothermal water from Mountain Home test well MH-2B: Preliminary Results, GRC Transactions, v. 36, p. 689-692.

Langmuir, D., 1997, Aqueous environmental geochemistry, Prentice Hall, New Jersey, 600 p.

Lindholm, G.F., 1996, Summary of the SRP Regional Aquifer-System Analysis in Idaho and Eastern Oregon, U.S. Geological Survey Professional Paper 1408-A, 68 p.

Leach, T.M., Rodgers, K.A., 1978, Metasomatism in the Wairere serpentinite, King Country, New Zealand, Mineralogical Magazine, v. 42, p. 45-62.

Lewis, R.E., and Stone, M.A.J., 1988, Geohydrologic data from a 4,403 foot geothermal test hole, Mountain Home Air Force Base, Elmore County, Idaho, USGS Open-file report 1988-166, 34 p.

Lewis, R.S., Link, P.K., Stanford, L.R., and Long, S.P., compilers, 2012, Geologic Map of Idaho-Geologic Map 9, Idaho Geological Survey, Scale 1:24,000.

Link, P.K. and Phoenix, E.C., 1996, Rocks Rails & Trails, 2nd Edition: Idaho Museum of Natural History, 194 p.

Mabey, D.R., 1976, Interpretation of a gravity profile across the western Snake River Plain, Idaho, Geology, v. 4, p. 53-55.

Mabey, D.R., 1978, Regional gravity and magnetic anomalies in the eastern Snake River Plain, Idaho, U.S. Geological Survey Journal of Research, v. 6, p. 553-562.

Mabey, D.R., 1982, Geophysics and tectonics of the Snake River Plain, Idaho, *in* Bill Bonnichsen and R.M. Breckenridge, eds., Cenozoic Geology of Idaho, Idaho Bureau of Mines and Geology Bulletin 26, p. 139-153.

Macpherson C. G., Hilton D. R., and Hammerschmidt, K., 2010, No slab-derived CO_2 in Mariana Trough back-arc basalts: implications for carbon subduction and for temporary storage of CO_2 beneath slow spreading ridges, Geochimica et. Cosmochimica Acta v. 11, p. 11.

Marini, L., 2000, Geochemical techniques for the exploration and exploitation of geothermal energy, Laboratorio di Geochimica, Universita degli di Genova, Genova, Italia, 82 p.

Mazurek, J., 2004, Genetic controls on basalt alteration within the Eastern Snake River Plain Aquifer System, Idaho [M.S. Thesis]: Department of Geosciences, Idaho State University, 227 p.

McCrea, J.M., 1950, On the isotopic chemistry of carbonates and a paleotemperature scale, Journal of Chemical Physics, v. 18, p. 849-857.

McLing, T.L., Smith, R.W., and Johnson, T.M., 2002, Chemical characteristics of thermal water beneath the eastern Snake River Plain: in Geology, Hydrogeology, and Environmental Remediation S Idaho Engineering and Environmental Laboratory, Eastern Snake River Plain, Idaho, Link, P.K. and L.L. Mink, editors: Geological Society of America Special Paper, 353, p. 205-211.

Moller, S.K., 1969, Xonotlite-, pectolite-, and natrolite-bearing fracture veins in volcanic rocks from Nugssuaq, West Greenland, Geological Survey of Greenland, v. 80, p. 4-20.

Moore, D.M., and Reynolds, R.C., 1997, X-ray diffraction and the identification and analysis of clay minerals 1st edition, Oxford University Press, 400 p.

Muffler, L.J.P., White, D.E., Truesdell, A.H., 1971, Hydrothermal explosion craters in Yellowstone National Park, Geological Society of America Bulletin v. 82, p.723-740.

Mutonga, M.W., Sveinbjornsdottir, A., Gislason, G., and Amannsson, H., 2010, The isotopic and chemical characteristics of geothermal fluids in Hengill Area, SW Iceland (Hellisheidi, Hveragerdi and Nesjavellir fields), *in* Proceedings of the World Geothermal Congress, Bali, Indonesia, p. 1-13.

Naboko, S.I., 1970, Facies of hydrothermally altered rocks of Kamchatka Kurile volcanic arc, Pacific Geology, v. 2, p. 23-27.

Nairn, I.A., Wiradiradja, S., 1980, Late Quaternary hydrothermal explosion breccias at Kawerau Geothermal Field New Zealand, Bulletin Volcanologique, v. 43, p. 1-13.

Negraru, P.T., Blackwell, D., and Richards, M., 2009, Texas Heat Flow Patterns, American Association of Petroleum Geologists Search and Discovery Article #80048, 9 p.

Nesse, W.D., 2003, Introduction to optical mineralogy: third edition, Oxford University Press, 370 p.

Nielson, D.L., Delahunty, C., and Shervais, J.W., 2012, Geothermal Systems in the Snake River Plain, Idaho, Characterized by the Hotspot Project, Geothermal Resources Council Transactions, v. 36, p. 727-730.

Nielson, D.L., and Shervais, J.W., 2014, Conceptual Model for Snake River Plain

Geothermal Systems, Proceedings Thirty-Ninth Workshop on Geothermal Reservoir Engineering Stanford University, Stanford, California, February 24-26, 2014 SGP-TR-202, 7 p.

Nielson, D.L., Shervais, J.W., Evans, J.P., Liberty, L., Garg, S.K., Glen, J., Visser, C., Dobson, P., Gasperikova, E., and Sonnenthal, E., 2015, Geothermal Play Fairway Analysis of the Snake River Plain, Idaho. Proceedings Fortieth Workshop on Geothermal Reservoir Engineering, Stanford University, Stanford, California, January 26-28, 2015 SGP-TR-204, 9 p.

O'Neil, J.R., Clayton, R.N., and Mayeda, T.K., 1969, Oxygen isotope fractionation in divalent metal carbonates, Journal of Chemical Physics, v. 51, no. 12, 12 p.

O'Neil, J.R., Adami, L.H., and Epstein, S., 1975, Revised value for the ^{18}O fractionation between CO_2 and H_2O at 25°C, U.S. Geological Survey Journal of Research, v. 3 #5 p. 623-624.

Pierce, K.L., and L.A. Morgan, 1992, The track of the Yellowstone hot spot: Volcanism, faulting, and uplift, *in* P.K. Link, M.A. Kuntz, and L.B. Platt, eds., Regional Geology of Eastern Idaho and Western Wyoming, Geological Society of America Memoir 179, 53 p.

Piper, A.M., 1944, A graphic procedure in the geochemical interpretation of water analysis, American Geophysical Union Transactions, v. 25, p. 914–923.

Roberson, H.E., Reynolds Jr., R.C., and Jenkins, D. M., 1999, Hydrothermal synthesis of corrensite: A study of the transformation of saponite to corrensite, Clays and Clay Minerals, v. 47, p. 212-218.

Roedder, E., 1984, Fluid inclusions, Reviews in Mineralogy, v. 12, Mineralogical Society of America, 644 p.

Rummel, F., and Kappelmeyer, O., 1993, Geothermal energy-future energy source? Verlag, C.F. Muller Karlsruhe, 98 p.

Seki, Y., Onuki, H., Okumura, K., and Takashima, I., 1969, Zeolite distribution in the Katayama geothermal area, Onikobe, Japan, Japanese Journal of Geology and Geography, v. 40, p. 63-79.

Sharp, Z., 2007, Principles of stable isotope geochemistry, New Jersey, Pearson Prentice Hall, 153 p.

Shervais, J.W., Gaurav Shroff, S.K. Vetter, S.M., Hanan, B.B., and McGee, J.J., 2002, Origin and evolution of the western Snake River Plain: Implications from stratigraphy, faulting, and the geochemistry of basalts near Mountain Home, Idaho, *in* Bill Bonnichsen, C.M. White, and Michael McCurry, eds., Tectonic and Magmatic Evolution of the Snake River Plain Volcanic Province, Idaho Geological Survey Bulletin 30, p. 343-361.

Shervais, J.W. and Vetter, S.K., 2009, High-K alkali basalts of the Western Snake River Plain (Idaho): Abrupt transition from tholeiitic to mildly alkaline plume-derived basalts, Journal of Volcanology and Geothermal Research, v. 188 p. 141-152.

Shervais, J.W., Schmitt, D.R., Nielsen, D.L., Evans, J.P., Christiansen E.H., Morgan, L., Shanks, W.C.P., Prokopenko, A.A., Lachmar, T., Liberty, L., Blackwell, D.D., Glen, J.M., Champion, D., Potter, K.E., and Kessler, J.A., 2013, First results from

Hotspot: The Snake River Plain Scientific Drilling Project, Idaho, U.S.A., Scientific Drilling, no. 15, 10 p.

Shervais, J.W., Evans, J.P., Schmitt, D.R., Christiansen, E.H., and Prokopenko, A., 2014, The Snake River Geothermal Drilling Project, EOS, Transactions American Geophysical Union, v. 95, p. 85-86.

Sigvaldason, G.E., 1963, Epidote and related minerals in two geothermal drill holes, Reykjavik and Hveragerdi, Iceland, U.S. Geological Survey Professional Paper 450-E, p. 77-79

Simmons, S.F., Christenson, B.W., 1994, Origins of calcite in a boiling geothermal system, American Journal of Science, v. 294, p. 361-400.

Stroncik, N.A., and Schmincke, H.U., 2002, Palagonite-a review, International Journal of Earth Sciences, v. 91, p. 680-697.

Thilo, E., and Funk, H., 1950, Uber einige chemische Eigenschaften des Pectoliths, $Ca_2Na(HSi_30_8)$, und seine Synthese, Zeits. Inorganic Chemistry, v. 261, p. 185-191.

Turcotte, D.L., and Schubert, G., 2002, Geodynamics 3rd Edition, University Press.

Wheeler, J., 2013, Clay mineralogy of the MH-2 core, Snake River Plain, Idaho, [Senior Capstone Project] Vassar College 239 p.

White, C.M. and Hart, W.K., 2002 Geochemical and Sr-isotopic variations in western Snake River Plain basalts, Idaho. In Bonnichsen, B., White, C.M., McCurry, M., (eds.), Tectonic and Magmatic Evolution of the Snake River Plain Volcanic Province. Idaho Geological Survey Bulletin, v. 30, p. 329–342.

Whitehead, R.L., 1994, Ground water atlas of the United States, Idaho, Oregon, Washington, U.S. Geological Survey Publication HA 730-H, 33 p.

Wood, S.H., Clemens, D.M., 2002, Geologic and tectonic history of the western Snake River Plain, Idaho and Oregon, in Bonnichsen, B., White, C.M., McCurry, M., (eds) Tectonic and magmatic evolution of the Snake River Plain Volcanic Province, Idaho Geological Survey Bulletin, v. 30, p. 69-103.

Wood, W.W., and Low, W.H., 1986, Aqueous geochemistry and diagenesis in the eastern Snake River Plain aquifer system, Idaho, Geological Society of America Bulletin, v. 97, p. 1456-1466.

Yagi, K., Kikuchi, T., and Kakuta, H., 1968, Thermal decomposition of pectolite and its hydrothermal synthesis, Journal of the Faculty of Science, Hokkaido University, Series 4 Geology and Mineralogy, v. 14, p. 123-134.

Young, H. W., 1977, Reconnaissance of ground water resources in the Mountain Home Plateau Area, Southwest Idaho: United States Geological Survey Water Resources Investigations Open-File Report 77-108, 40 p.

APPENDICES

Appendix A. X-RAY DIFFRACTION PATTERNS

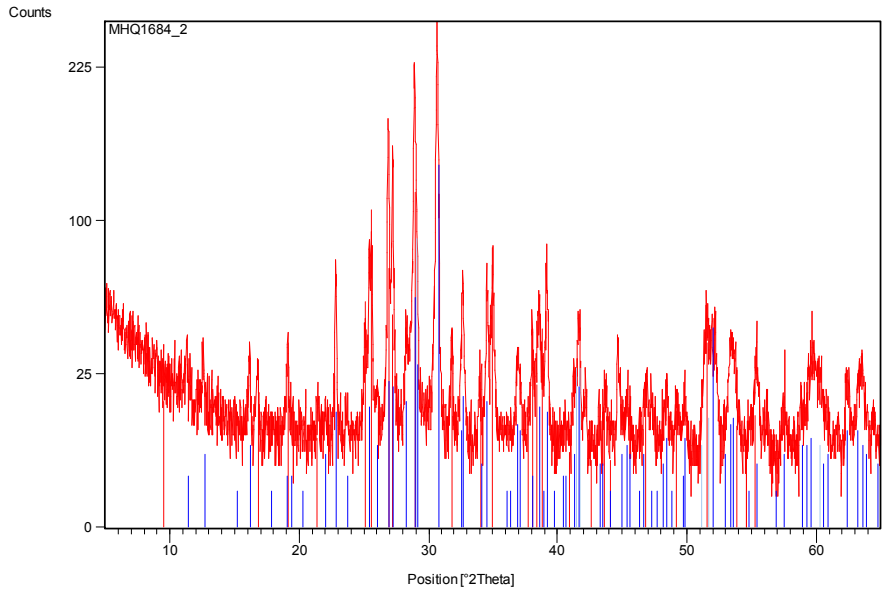

Figure A1: X-ray diffraction pattern from 1684 mbgs of prehnite and pectolite

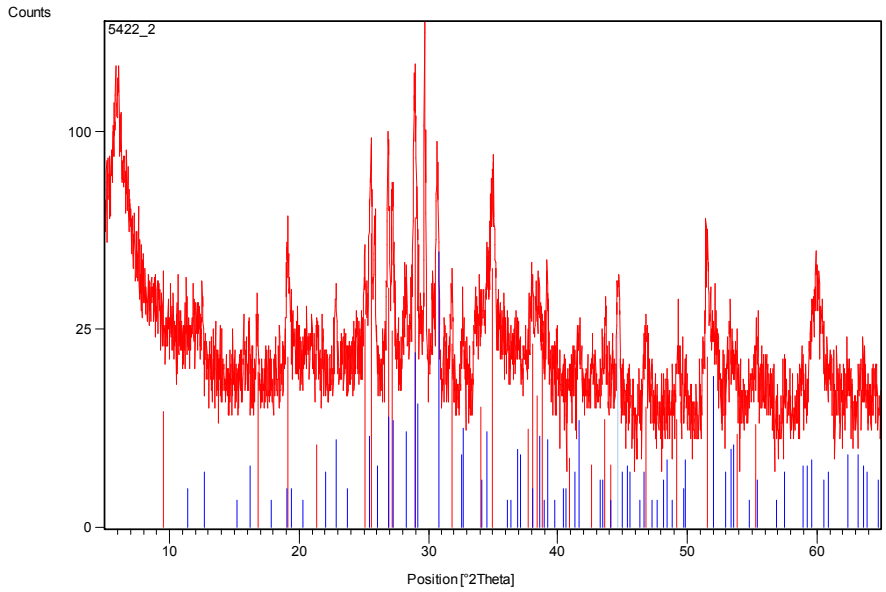

Figure A2: X-ray diffraction pattern from 1653 mbgs of prehnite and pectolite

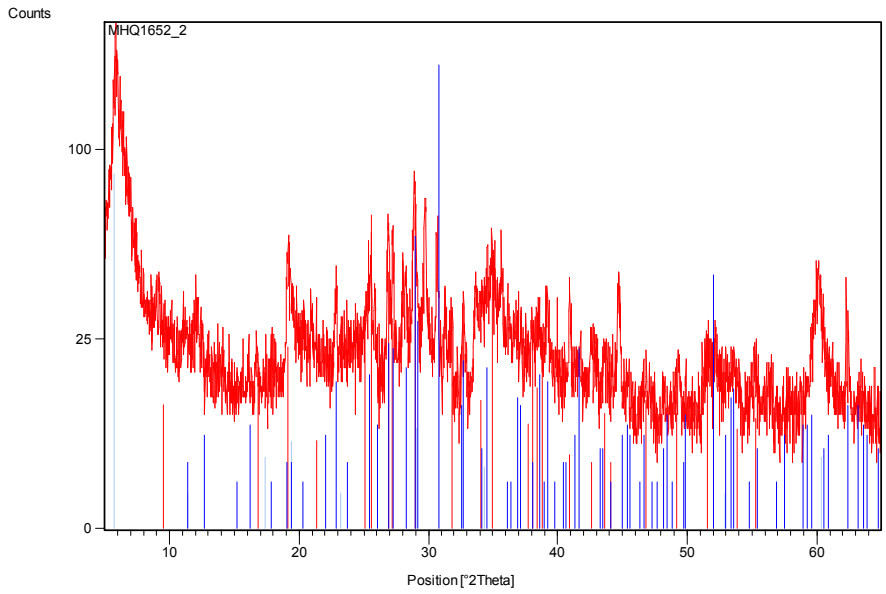

Figure A3: X-ray diffraction pattern from 1652 mbgs of prehnite and pectolite

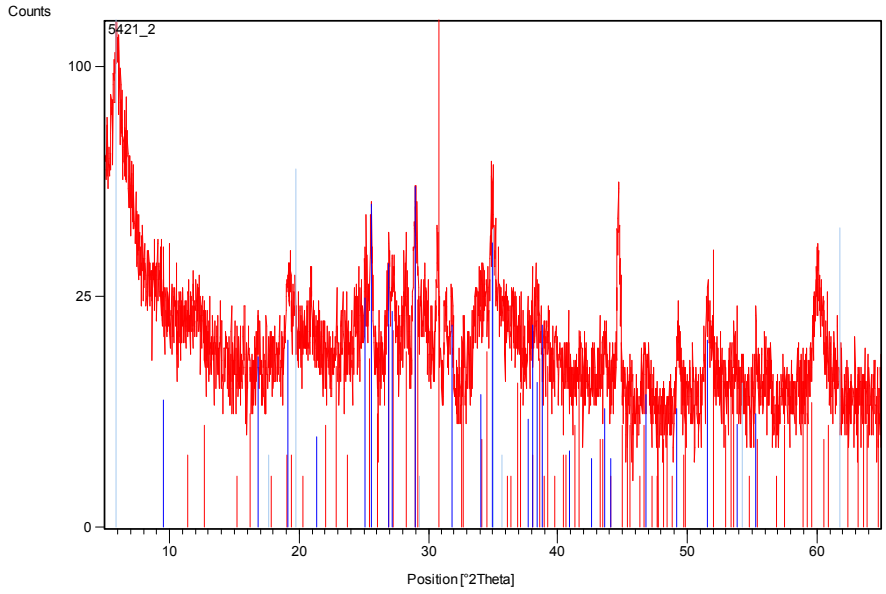

Figure A4: X-ray diffraction pattern from 1652 mbgs of prehnite and pectolite

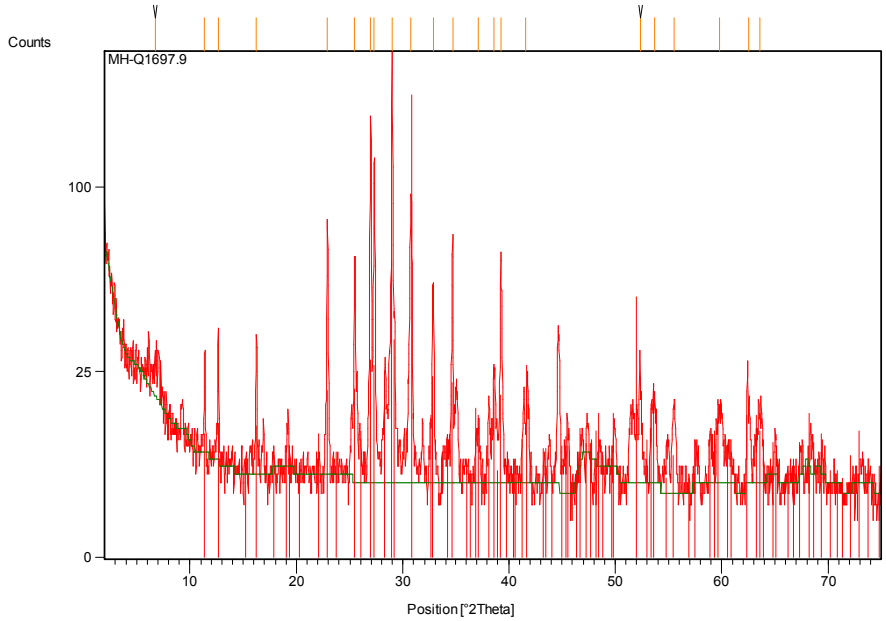

Figure A5: X-ray diffraction pattern from 1697 mbgs of pectolite

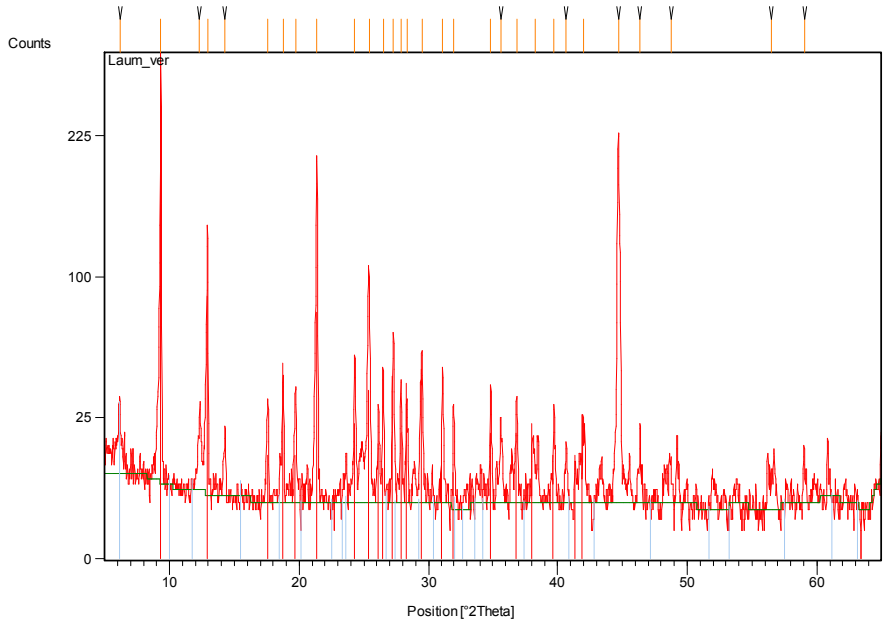

Figure A6: X-ray diffraction pattern of laumontite from crystals gathered from various depths

Appendix B. STABLE ISOTOPE DATA

Table A1: Table of all data collected for stable isotope analysis of calcites from 1709-1807 mbgs

Depth (mbgs)	$\delta^{13}C$ ‰ vs. PDB	$\delta^{18}O$ ‰ vs. PDB	$\delta^{18}O$ ‰ vs. SMOW
1709.05	-5.50	-16.97	13.42
1709.20	-4.83	-17.31	13.06
1709.21	-3.84	-18.39	11.96
1709.23	-4.42	-17.76	12.61
1709.33	-4.20	-18.12	12.23
1711.06	-5.81	-16.20	14.21
1711.14	-4.94	-18.06	12.29
1711.67	-4.07	-17.33	13.04
1713.21	-3.18	-18.12	12.23
1713.49	-3.68	-17.37	13.00
1714.13	-4.27	-17.00	13.38
1714.42	-4.82	-17.51	12.86
1715.15	-3.19	-18.97	11.36
1716.21	-3.52	-19.45	10.86
1716.21	-3.32	-17.56	12.81
1716.35	-3.84	-17.53	12.84
1716.35	-4.11	-19.59	10.71
1717.37	-5.20	-17.58	12.79
1717.92	-7.21	-17.92	12.44
1718.05	-3.50	-19.56	10.75
1718.08	-3.77	-19.86	10.43
1718.10	-5.85	-17.86	12.49
1718.67	-6.66	-17.68	12.69
1718.99	-6.84	-16.94	13.44
1722.10	0.66	-8.11	22.55
1722.89	0.15	-9.01	21.62
1723.39	0.88	-8.44	22.21
1724.15	-1.94	-17.11	13.27
1725.03	-0.71	-13.95	16.53
1725.56	-0.01	-9.99	20.61
1727.51	-2.83	-19.44	10.87
1730.05	-3.23	-19.89	10.41
1730.24	-3.09	-19.94	10.36
1730.65	-2.68	-18.22	12.13
1731.26	-2.70	-18.49	11.85

Depth (mbgs)	$\delta^{13}C$ ‰ vs. PDB	$\delta^{18}O$ ‰ vs. PDB	$\delta^{18}O$ ‰ vs. SMOW
1731.46	-3.04	-17.93	12.43
1731.49	-3.07	-17.61	12.75
1731.51	-3.40	-20.16	10.13
1731.69	-3.77	-18.81	11.52
1731.96	-3.50	-18.88	11.45
1732.00	-3.75	-18.52	11.82
1732.15	-3.52	-19.08	11.24
1732.17	-3.68	-18.76	11.57
1732.17	-3.70	-19.02	11.30
1732.20	-3.57	-18.97	11.35
1732.33	-3.75	-19.19	11.13
1732.40	-3.96	-19.09	11.23
1733.43	-4.12	-19.00	11.32
1733.67	-4.36	-18.43	11.91
1734.56	-4.65	-19.35	10.97
1734.94	-3.92	-19.30	11.01
1735.39	-4.63	-19.37	10.94
1735.70	-4.81	-19.48	10.83
1735.74	-3.61	-19.53	10.78
1735.83	-4.21	-18.97	11.36
1735.93	-2.05	-17.88	12.48
1736.00	-3.80	-18.32	12.03
1736.39	-3.67	-18.17	12.18
1736.63	-4.08	-19.38	10.93
1736.89	-4.16	-18.39	11.95
1737.16	-3.77	-18.58	11.76
1737.19	-3.34	-17.57	12.79
1737.77	-3.12	-19.09	11.23
1738.07	-5.65	-19.27	11.05
1738.41	-3.98	-18.87	11.46
1738.52	-4.04	-19.62	10.69
1738.58	-3.89	-19.90	10.39
1738.60	-4.62	-19.15	11.17
1738.64	-4.15	-19.78	10.52
1738.67	-3.41	-19.27	11.05
1738.80	-3.60	-19.56	10.75
1738.96	-3.84	-19.43	10.88

Depth (mbgs)	$\delta^{13}C$ ‰ vs. PDB	$\delta^{18}O$ ‰ vs. PDB	$\delta^{18}O$ ‰ vs. SMOW
1739.29	-4.23	-19.26	11.06
1739.39	-4.79	-19.01	11.32
1739.58	-4.54	-18.97	11.35
1739.68	-4.89	-18.91	11.41
1739.98	-3.69	-18.75	11.58
1740.07	-4.58	-19.32	10.99
1740.54	-4.51	-19.42	10.89
1741.02	-4.31	-19.92	10.38
1741.63	-4.25	-20.36	9.92
1742.39	-4.58	-18.86	11.47
1744.98	-2.72	-17.91	12.44
1745.59	-4.79	-19.68	10.62
1745.89	-3.74	-19.77	10.52
1746.20	-3.92	-18.26	12.08
1746.50	-5.13	-17.19	13.19
1746.66	-3.58	-20.34	9.94
1746.81	-3.12	-20.11	10.17
1747.65	-3.84	-15.94	14.48
1747.88	-3.47	-19.70	10.60
1748.22	-4.27	-18.71	11.62
1748.33	-3.91	-19.02	11.30
1748.49	-3.32	-18.17	12.18
1748.55	-2.00	-18.18	12.17
1748.64	-3.99	-19.57	10.73
1748.70	-3.27	-20.28	10.00
1749.09	-3.48	-19.74	10.56
1749.40	-3.49	-20.54	9.74
1750.22	-2.44	-18.94	11.39
1751.08	-4.34	-19.38	10.93
1751.38	-3.99	-19.29	11.02
1751.69	-3.96	-19.25	11.07
1752.07	-3.91	-19.41	10.90
1753.51	-4.07	-19.22	11.09
1753.67	-3.51	-19.54	10.77
1754.58	-4.63	-18.54	11.80
1754.73	-4.58	-19.08	11.24
1755.27	-3.66	-19.59	10.71

Depth (mbgs)	$\delta^{13}C$ ‰ vs. PDB	$\delta^{18}O$ ‰ vs. PDB	$\delta^{18}O$ ‰ vs. SMOW
1756.60	-3.53	-19.13	11.19
1757.58	-4.09	-18.82	11.51
1760.35	-4.28	-18.44	11.90
1762.64	-4.24	-18.90	11.43
1762.77	-3.43	-17.48	12.89
1767.84	-3.90	-18.67	11.67
1772.46	-3.53	-18.29	12.05
1773.12	-3.24	-18.33	12.01
1774.34	-4.49	-18.69	11.64
1774.76	-4.27	-18.28	12.06
1775.22	-3.87	-18.84	11.49
1778.98	-3.43	-18.89	11.44
1780.01	-3.87	-19.83	10.47
1785.09	-4.14	-19.33	10.99
1786.23	-3.17	-18.68	11.65
1787.04	-3.57	-19.83	10.47
1789.00	-3.73	-20.34	9.94
1790.02	-3.43	-18.34	12.00
1790.82	-3.65	-20.02	10.27
1796.17	-3.90	-19.27	11.04
1797.97	-3.57	-18.28	12.06
1798.93	-3.37	-19.48	10.83
1799.23	-3.57	-19.66	10.64
1803.78	-4.42	-18.33	12.01
1806.37	-3.92	-18.83	11.49
1806.40	-3.66	-18.37	11.98
1806.42	-3.85	-19.02	11.30
1807.49	-4.42	-18.76	11.57